

Lattice-Boltzmann Simulations of Particle-Fluid Suspensions

A. J. C. Ladd¹ and R. Verberg¹

Received November 11, 2000; revised April 13, 2001

This paper reviews applications of the lattice-Boltzmann method to simulations of particle-fluid suspensions. We first summarize the available simulation methods for colloidal suspensions together with some of the important applications of these methods, and then describe results from lattice-gas and lattice-Boltzmann simulations in more detail. The remainder of the paper is an update of previously published work,^(69, 70) taking into account recent research by ourselves and other groups. We describe a lattice-Boltzmann model that can take proper account of density fluctuations in the fluid, which may be important in describing the short-time dynamics of colloidal particles. We then derive macrodynamical equations for a collision operator with separate shear and bulk viscosities, via the usual multi-time-scale expansion. A careful examination of the second-order equations shows that inclusion of an external force, such as a pressure gradient, requires terms that depend on the eigenvalues of the collision operator. Alternatively, the momentum density must be redefined to include a contribution from the external force. Next, we summarize recent innovations and give a few numerical examples to illustrate critical issues. Finally, we derive the equations for a lattice-Boltzmann model that includes transverse and longitudinal fluctuations in momentum. The model leads to a discrete version of the Green-Kubo relations for the shear and bulk viscosity, which agree with the viscosities obtained from the macro-dynamical analysis. We believe that inclusion of longitudinal fluctuations will improve the equipartition of energy in lattice-Boltzmann simulations of colloidal suspensions.

KEY WORDS: Lattice-Boltzmann; suspensions; simulations of colloids; hydrodynamic interactions.

¹Chemical Engineering Department, University of Florida, Gainesville, Florida 32611-6005.
e-mail: ladd@che.ufl.edu

1. INTRODUCTION

The flow of a dense suspension of colloidal particles is difficult to quantify experimentally or to predict theoretically. Rheological properties of colloidal suspensions are sensitive to variations in inter-particle forces, which can often result from small changes in solvent conditions. Although there is an extensive literature of empirical correlations describing the rheology of colloidal suspensions under certain flow conditions, a fundamental understanding of suspension rheology and dynamics is limited to simple model systems. Numerical simulations can aid in extending our understanding to more complex colloidal suspensions. First; they can provide a test bed for theoretical ideas, allowing them to be evaluated in a simpler and more rigorous environment than is possible experimentally. Second; they can be used to isolate and investigate different physical effects. Third; they can provide more detailed and direct information on the particle dynamics and structure than is typically possible with experimental measurements. In this article we will briefly review the simulation techniques available for particle suspensions, and then focus on algorithms derived from the lattice-Boltzmann model of the fluid phase. Some of the material presented here is a summary of published work, particularly refs. 69 and 70. However, the methodology has been modified to take account of density fluctuations in the fluid, which may be important to the short-time dynamics of colloidal particles, and also to consider more carefully the effects of external forces. Recent advances and ongoing technical issues will also be discussed. Finally, we will make some rough estimates of the computational costs of typical simulations.

1.1. Hydrodynamic Interactions

The canonical model of a colloidal suspension is a dispersion of identical rigid spheres suspended in an incompressible Newtonian fluid. The equilibrium distribution of particle positions is identical to that of the hard-sphere fluid, the fundamental model for all simple molecular liquids. However, the dynamical properties of a hard-sphere suspension are quite different from those of a hard sphere fluid, with hydrodynamic interactions replacing particle-particle collisions as the dominant mechanism for momentum transfer. From a molecular point of view, hydrodynamic interactions are the result of correlated momentum transfer from a colloidal particle to solvent molecules, and then from the solvent molecules to another colloidal particle.⁽²⁹⁾ Nevertheless, since the length-scale and time-scale separations between colloidal particles and solvent molecules are at least two orders of magnitude, we can usually treat the solvent as a con-

tinuum fluid,⁽⁹⁾ whose dynamics are described by the Navier–Stokes equations for the mass density, ρ , and momentum density, $\rho\mathbf{u}$:

$$\begin{aligned}\partial_t \rho + \nabla \cdot (\rho \mathbf{u}) &= 0 \\ \partial_t (\rho \mathbf{u}) + \nabla \cdot (\rho \mathbf{u} \mathbf{u}) + \nabla p &= \nabla \cdot \boldsymbol{\sigma} + \nabla \cdot \boldsymbol{\sigma}^f,\end{aligned}\quad (1)$$

where p is the thermodynamic pressure, $\boldsymbol{\sigma}$ is the viscous stress tensor, and $\boldsymbol{\sigma}^f$ is the fluctuating stress. If we make the reasonable assumption that viscous dissipation is small and does not affect the thermodynamic state, then the pressure follows an adiabatic equation of state

$$p(\rho) = p_0 + (\rho - \rho_0) \left(\frac{\partial p}{\partial \rho} \right)_{s=s_0} + \dots, \quad (2)$$

where p_0 and s_0 are the pressure and entropy at the reference density ρ_0 . Thus for small density fluctuations, the equation of state of a liquid or a gas, $\nabla p = c_s^2 \nabla \rho$, differ only in the speed of sound $c_s = \sqrt{(\partial p / \partial \rho)_s}$. The viscous stresses are characterized by the shear and bulk viscosities, η and η_v , which we will take to be constants, independent of thermodynamic state and flow conditions:

$$\boldsymbol{\sigma} = \eta [(\nabla \mathbf{u}) + (\nabla \mathbf{u})^\dagger - \frac{2}{3} (\nabla \cdot \mathbf{u}) \mathbf{1}] + \eta_v (\nabla \cdot \mathbf{u}) \mathbf{1}, \quad (3)$$

where $(\nabla \mathbf{u})^\dagger$ is the matrix transpose of $(\nabla \mathbf{u})$, and $\mathbf{1}$ is the unit matrix.

On scales of interest to colloidal suspensions, fluctuations in thermodynamic variables cannot be ignored; in particular, Brownian motion of colloidal particles is driven by fluctuations in the fluid stress tensor. The amplitude of these fluctuations can be calculated from statistical thermodynamics,⁽⁷⁸⁾ and their time evolution is described by the laws of linear hydrodynamics.⁽⁷⁷⁾ On colloidal time scales ($> 10^{-8}$ s), the components of $\boldsymbol{\sigma}^f$ behave as Gaussian random variables with zero mean and variance:⁽⁷⁷⁾

$$\begin{aligned}\langle \sigma_{\alpha\beta}^f(\mathbf{r}_1, t_1) \sigma_{\gamma\delta}^f(\mathbf{r}_2, t_2) \rangle \\ = 2k_B T [\eta (\overline{\delta_{\alpha\gamma} \delta_{\beta\delta}} + \overline{\delta_{\alpha\delta} \delta_{\beta\gamma}}) + \eta_v \delta_{\alpha\beta} \delta_{\gamma\delta}] \delta(\mathbf{r}_1 - \mathbf{r}_2) \delta(t_1 - t_2),\end{aligned}\quad (4)$$

where $\overline{\delta_{\alpha\gamma} \delta_{\beta\delta}} = \delta_{\alpha\gamma} \delta_{\beta\delta} - \frac{1}{3} \delta_{\alpha\beta} \delta_{\gamma\delta}$ is traceless in $\alpha\beta$ and $\gamma\delta$. It should be noted that Eq. 4 does not describe the instantaneous fluctuations in stress on a molecular time scale. Rather it expresses the time-dependent relaxation of stress fluctuations in a form that is local in space and time, yet consistent with the Green–Kubo expressions for the shear and bulk viscosities. Such expressions are valid on length and time scales that are large compared with molecular scales; colloidal suspensions satisfy both these requirements.

To complete the specification of the fluid-dynamical problem, boundary conditions at the particle-fluid interfaces are needed. It is universally assumed that a stick boundary condition exists between the solid particle surfaces and the fluid. In other words the velocity of the fluid adjacent to a particle surface is equal to the local velocity of the surface at that point; *i.e.*

$$\mathbf{u}(\mathbf{r}) = \mathbf{U} + \mathbf{\Omega} \times (\mathbf{r} - \mathbf{R}), \quad (5)$$

for all points \mathbf{r} on the surface S , where \mathbf{U} , $\mathbf{\Omega}$, \mathbf{R} are the particle velocity, angular velocity, and position. Experimental evidence suggests that this assumption is quantitatively correct for particles larger than about $30nm$.⁽¹¹⁸⁾ Finally, the forces and torques on the colloidal particles are obtained by integrating the stress over the particle surface;

$$\begin{aligned} \mathbf{F}(t) &= \oint_S \mathbf{t}(\mathbf{r}) d\mathbf{r} \\ \mathbf{T}(t) &= \oint_S \mathbf{r} \times \mathbf{t}(\mathbf{r}) d\mathbf{r}, \end{aligned} \quad (6)$$

where $\mathbf{t} = -p\mathbf{n} + \boldsymbol{\sigma} \cdot \mathbf{n} + \boldsymbol{\sigma}^f \cdot \mathbf{n}$ is the surface traction and \mathbf{n} is the outward surface normal. The particle dynamics can then be calculated by solving Newton's equations of motion, including any inter-particle forces derived from a conservative potential.

The above formulation is convenient for developing many of the techniques for simulating colloidal suspensions, including lattice-Boltzmann and finite-element methods. However, there is an alternate formulation that expresses the time evolution of the particle positions as a set of coupled stochastic differential equations,⁽¹⁰⁰⁾

$$d\mathbf{R}^N = \mathbf{A}^N(\mathbf{R}^N) dt + \mathbf{B}^{NN}(\mathbf{R}^N) \cdot d\mathbf{W}^N. \quad (7)$$

\mathbf{A}^N and \mathbf{B}^{NN} are a $3N$ vector of deterministic coefficients and a $3N \times 3N$ matrix of stochastic coefficients; the components of \mathbf{W}^N are independent Gaussian random variables with zero mean and variance dt . With the appropriate choice of \mathbf{A}^N and \mathbf{B}^{NN} ,⁽¹⁰⁰⁾ an ensemble average over many initial conditions is equivalent to a solution of the Smoluchowski equation, which describes the time evolution of the N -particle coordinate distribution function:

$$\partial_t P(\mathbf{R}^N, t) = \nabla^N \cdot \mathbf{D}^{NN}(\mathbf{R}^N) \cdot \{[\nabla^N \beta \Phi(\mathbf{R}^N)] + \nabla^N\} P(\mathbf{R}^N, t). \quad (8)$$

The hydrodynamic mobilities $\beta \mathbf{D}^{NN}(\mathbf{R}^N)$, required to determine both \mathbf{A}^N and \mathbf{B}^{NN} (Eq. 7), can be calculated from the steady-state hydrodynamic interactions between the particles, using the equations for Stokes flow:

$$\begin{aligned}\nabla \cdot \mathbf{u} &= 0 \\ \nabla p &= \eta \nabla^2 \mathbf{u}.\end{aligned}\tag{9}$$

In contrast with the previous formulation, here the fluctuations have been incorporated directly into the particle dynamics, rather than into the equations for the fluid motion. This approach is not quite as general as the one given earlier; in particular it is limited to low Reynolds number flows, or to particles less than $100 \mu\text{m}$ in size. Moreover, the assumption of steady state hydrodynamics makes it impossible to simulate the temporal and spatial development of hydrodynamic interactions, which has been a subject of growing interest since the development of experimental probes to study sub-microsecond time scales.^(40, 123) However, it is the foundation for several important computational methods, including Brownian dynamics⁽³³⁾ and Stokesian dynamics.⁽¹²⁾

1.2. Suspension Rheology

The rheological characteristics of hard-sphere suspensions have been explained recently by a combination of theoretical analysis^(4, 11, 119) and numerical simulation.^(17, 39, 92, 101) The viscosity of hard-sphere suspensions is composed of a frequency-independent hydrodynamic stress, coming from the added resistance to shear caused by fluid flow around the particles, and a frequency-dependent Brownian stress arising from viscous resistance to fluctuations in particle position. Theoretical calculations of the viscoelastic response of hydrodynamic and Brownian stresses^(11, 119) are in good agreement with experimental data.^(117, 118)

Under a steady external shear rate $\dot{\gamma}$, the suspension first exhibits shear thinning,^(39, 101) caused by a reduction in Brownian stress, which culminates in a second Newtonian region at a Peclet number, $Pe = \dot{\gamma} a^2 / D$, around 10. At Peclet numbers larger than 10–100, the effects of Brownian motion are small and the microstructure of the suspension is determined by the external shear rate. In this region the hydrodynamic stress increases rapidly, due to clustering of the particles into transient aggregates, so that the stress tensor is dominated by the lubrication forces exerted between particle surfaces close to contact.⁽⁹²⁾ It has been shown that the high-shear-rate behavior of an idealized hard-sphere suspension is singular,⁽¹³⁾ in that the viscosity increases without bound as the shear rate increases. The breakdown of this singular behavior is controlled by small additional effects, such as

short-range repulsive forces, which inhibit cluster formation.⁽¹⁷⁾ These important insights may eventually explain the sensitivity of the high-shear rate viscosity to small variations in inter-particle forces.

In attempting to develop a fundamental understanding of more complex suspensions, it is important to differentiate between new physical effects and well known physical effects manifested in unexpected situations. For example, the rheology of hard-sphere systems was difficult to comprehend until numerical simulations⁽¹⁰¹⁾ showed that it was a combination of the different shear-rate dependence of the hydrodynamic and Brownian stresses. Similarly, numerical simulations^(17, 105) are leading to an increased understanding of the role of ordering in determining the rheology of suspensions of charged particles. However, we note that it is not yet possible to predict the rheology of suspensions of charged or polymer coated particles with the same precision as hard-sphere dispersions.⁽¹⁷⁾

It is clear that numerical simulations will be crucial in obtaining a fundamental understanding of the dynamics of colloidal suspensions. However, simulations are limited by their algorithmic complexity, which makes the computer programs difficult to implement and use, and the enormous computational resources that are necessary to simulate systems of macroscopic size. Nevertheless, there are now several different methods that can be used to simulate suspensions of solid particles under a variety of different flow conditions. After a brief review of the available simulation methods, we will present a more detailed review of applications of methods based on the lattice-Boltzmann model of the fluid. Then we will describe the basic algorithms in some detail, and give several examples to illustrate the accuracy and efficiency of the method. We will also describe some recent technical innovations that can further improve the computational efficiency.

2. SIMULATION METHODS

Numerical simulations that take explicit account of the hydrodynamic forces between the suspended particles are becoming useful tools for studying the dynamics of particle suspensions. Brownian dynamics,⁽³³⁾ the pioneering simulation method for colloidal suspensions and polymer solutions, is a stochastic simulation of the time evolution of the Smoluchowski equation (Eq. 8), typically using a first-order integration of the stochastic differential equations (Eq. 7). The crucial approximation in Brownian dynamics is the assumption that hydrodynamic interactions can be represented by a pairwise-additive sum of two-particle mobility tensors,⁽³³⁾ or ignored altogether. However, despite the oversimplified hydrodynamic interactions,

Brownian dynamics gives important qualitative insights into the dynamics of colloidal suspensions, and can be quantitative in some instances; for example dilute suspensions of charged particles.⁽¹⁰⁵⁾

2.1. Stokesian Dynamics

More accurate simulation techniques make use of a reformulation of the Stokes equations (Eq. 9) as an integral equation for the fluid velocity field generated by a prescribed force density \mathbf{f}_{ind} :

$$\mathbf{u}(\mathbf{r}) = \int_V \mathbf{T}(\mathbf{r} - \mathbf{r}') \cdot \mathbf{f}_{ind}(\mathbf{r}') d\mathbf{r}', \quad (10)$$

where $\mathbf{T}(\mathbf{r}) = (8\pi\eta r)^{-1} (\mathbf{1} + \hat{\mathbf{r}}\hat{\mathbf{r}})$ is the Oseen tensor, the Green's function for Stokes flow in an infinite domain. The force density is localized to the particle surfaces, so for spherical particles, the obvious (and optimal) solution is to expand the force density and velocity field in spherical harmonics. This leads to a linear system of equations, relating moments of the fluid velocity on the particle surfaces to moments of \mathbf{f}_{ind} . The hydrodynamic interactions used in Brownian dynamics are obtained by assuming that the force density is uniformly distributed over the particle surface. However, in the presence of other solid particles, the force density is redistributed so as to satisfy the boundary conditions for the fluid velocity on neighboring particle surfaces. The problem is analogous to the polarization of interacting charge distributions, and an exact solution requires an infinite hierarchy of multipole moments.

Stokesian dynamics^(12, 31) utilizes a much better approximation to the hydrodynamic interactions than Brownian dynamics, obtained by truncating the multipole hierarchy at the $L = 1$ order of spherical harmonics rather than $L = 0$. An important consequence of including particle torques and stresses (the $L = 1$ moments of \mathbf{f}_{ind}) is that the interactions between distant spheres are given exactly, even in the presence of an external shear. The other significant innovation of Stokesian dynamics was the incorporation of short-range "lubrication" forces. When two particles are near contact, the hydrodynamic interactions are dominated by forces originating from flow in the gap between the particles. Although hydrodynamic interactions are not additive in general, lubrication forces are an exception and can simply be added, pair by pair, to the far-field forces. Including lubrication forces in this way allows a truncated multipole expansion to accurately represent the hydrodynamic interactions in all particle configurations. This insight⁽³¹⁾ is of fundamental importance to simulations of particle suspen-

sions, extending beyond Stokesian dynamics and related algorithms. In practice, no general numerical method can afford the computational cost of resolving the flow in the narrow gaps between closely-spaced particles, so lubrication forces always require special treatment.

More accurate calculations of the hydrodynamic interactions are possible, extending approximate solutions of (Eq. 10) to higher order multipoles.⁽⁶⁶⁾ However, some properties, for example the permeability and sedimentation velocity, are slowly converging functions of L_{max} and the added computational cost is high, scaling as at least the 4th power of L_{max} . This approach has been used to calculate accurate values of the hydrodynamic transport coefficients of equilibrium configurations of hard spheres,⁽⁶⁷⁾ but not for dynamic simulations. At the present time, even Stokesian dynamics is too time consuming for dynamical simulations of more than a few hundred particles. A long-term solution may involve the adoption of hierarchical multipole (or fast multipole) methods,⁽¹⁰⁸⁾ which reduce the computation time for calculating the mobility matrix from $\mathcal{O}(N^2)$ to $\mathcal{O}(N)$ or $\mathcal{O}(N \ln N)$. Unfortunately a large number of particles are required before the asymptotic scaling is reached, so the impact of these innovations may be limited until further increases in computational power are realized. A completely different approximation makes use of the fact that for highly concentrated suspensions (solid volume fractions greater than 50%), the rheology is dominated by the lubrication forces. Thus it has been proposed that the long-range hydrodynamic interactions be ignored, and the mobility tensor calculated on the basis of lubrication forces alone.⁽³⁾ Within this lubrication approximation, it is possible to simulate the motion of a few thousand colloidal particles.⁽¹⁷⁾

Stokesian dynamics has limitations in addition to those imposed by computational cost. The suspending fluid is assumed to be Newtonian and to be flowing under conditions approximating Stokes flow ($Re = 0$). Moreover, the method is difficult to extend to suspensions of non-spherical particles, or to suspensions bounded by container walls. However, recent innovations are addressing many of these issues^(3, 7, 25, 26) and Stokesian dynamics remains a robust, physically-motivated algorithm, which is straightforward to use, although quite complicated to code. The Stokes equations (Eq. 10) can also be solved by boundary-element methods, which are more flexible than Stokesian dynamics and can be applied to non-spherical or deformable particles.^(81, 95, 102) However, boundary-element methods are even more computationally demanding than Stokesian dynamics; here the state-of-the-art is represented by simulations of approximately 100 deformable drops in a shear flow.⁽¹²⁷⁾

2.2. Time-Dependent Methods

The computational methods described so far have been based on the classical theory of suspensions,⁽⁵¹⁾ in which the hydrodynamic interactions are assumed to be fully developed; in other words, where there is a complete separation of time scales between the dynamics of the fluid and the motion of the solid particles. In reality, hydrodynamic interactions develop in time and space from purely local stresses generated at the solid-fluid surfaces, which then propagate throughout the fluid by diffusive momentum transport. Several computational schemes attempt to exploit this spatial locality to develop algorithms whose computational cost scales linearly with the number of particles; these include lattice-Boltzmann and finite-element methods, as well as particle-based schemes such as dissipative particle dynamics. However, for low Reynolds number flows, the computational gains arising from spatial locality are offset by the additional time scale required to follow the motion of the fluid.

Until recently, finite-element methods were unable to generate suitable computational grids for the complex geometries imposed by suspensions of solid particles. Although very accurate solutions were possible for individual particles,⁽³⁸⁾ results for multi-particle suspensions^(32, 44) were restricted to limited numbers of individual configurations, rather than dynamical simulations. However, recent advances in mesh generation techniques have made dynamical simulations feasible for both spherical and non-spherical particles.^(34, 35) Finite-element techniques are very flexible, in that they can incorporate inertia and non-Newtonian effects⁽⁶²⁾ into the fluid dynamics. On the other hand the algorithms are difficult to develop and code, and require massive computational resources to run problems of realistic scales. Finite-element methods have not yet been used to study the dynamics of colloidal suspensions, although it should be straightforward to include thermal fluctuations into the fluid stress tensor; random fluctuations with somewhat different statistics have already been introduced into a finite-difference code in the context of turbulence modeling.⁽⁷⁹⁾ Finite-element (or finite-difference) simulations can also be carried out on a uniform grid using embedded point forces to describe the solid-fluid boundary conditions;^(37, 47) front-tracking is a necessary complication when the particles are deformable.⁽¹¹⁵⁾ Uniform grids may eventually prove to be more efficient than irregular meshes, due to the computational costs and loss of accuracy inherent in re-meshing.

It has sometimes been suggested that a suspension can be modeled as a mixture of large and small particles, but in this case it is practically impossible to enforce the proper time scale separation between hydrodynamic interactions and particle diffusion. In a colloidal suspension, the time scale

of the hydrodynamic interactions, $\tau_H = \rho a^2 / \eta$, is much smaller than the time scale for colloidal particle diffusion, $\tau_D = a^2 / D$. By dimensional analysis we find that the ratio of these time scales is just the ratio of solvent molecule size, a_s , to colloidal particle size, a ;

$$\frac{\tau_H}{\tau_D} = \frac{\rho D}{\eta} \approx \frac{\rho k_B T}{\eta^2 a} \approx \frac{a_s}{a}. \quad (11)$$

Thus a large size ratio (at least 100 : 1) is required to obtain the separation of time scales that characterizes a colloidal suspension (as opposed to a molecular solution), making a fully molecular simulation prohibitively expensive. In dissipative particle dynamics⁽⁵⁸⁾ a combination of frictional and stochastic forces is used to introduce an additional time scale separation, independent of size ratio. It is not yet clear if this is completely successful.⁽⁴⁹⁾ Other quasi-particle methods, such as direct simulation Monte Carlo⁽⁸⁾ and smooth particle hydrodynamics,^(59, 93) can also be employed to model particle-fluid systems,^(94, 124) but algorithms for dynamic simulations have not yet been developed.

2.3. Lattice-Gases

The lattice-gas model⁽⁴²⁾ was introduced in an effort to overcome the computational barriers hindering simulations of high-Reynolds number flow. Although this supposition was quickly refuted,⁽⁹⁹⁾ it was also realized that lattice-gas methods might have substantial advantages over Stokesian dynamics for flows in porous media⁽¹⁰⁶⁾ and colloidal suspensions.⁽⁷³⁾ It could be shown that under certain conditions, the large-scale dynamics of a lattice-gas cellular automaton could be mapped onto the incompressible Navier–Stokes equations.^(41, 42) Moreover, for small deviations from equilibrium, the equations of fluctuating hydrodynamics (Eq. 1) could be derived⁽⁴¹⁾ from the intermediate-scale dynamics of the lattice gas. This connection offered the opportunity to simulate colloidal suspensions, with hydrodynamic interactions, but without the computational difficulties involved in calculating the eigenvectors and eigenvalues of the diffusion tensor.

The lattice-gas model is extraordinarily simple to program, and in its two-dimensional version, extremely efficient. The update rules can be written in a few lines of Boolean logic, which are sufficient to update W sites, where W is the word length of the computer. In the first step fluid particles are “collided”, which means the bits representing them are rearranged, subject to the constraint of mass and momentum conservation;

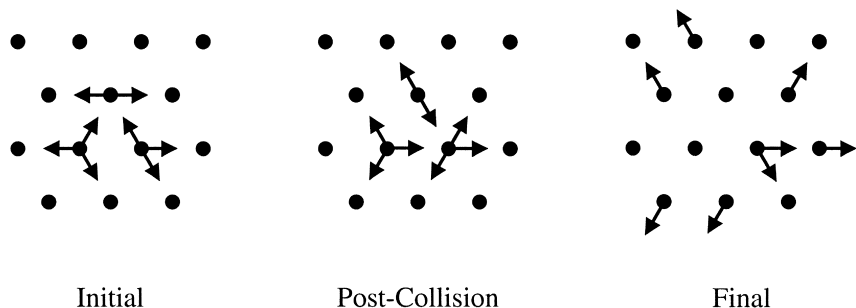


Fig. 1. Schematic representation of the FHP lattice-gas model. The sketch shows the evolution of a dilute lattice-gas through a single time step, from the initial state (a), through the collision step (b), to the final state (c).

examples of the possible collisions are shown in Fig. 1a-b. In the second step, particles are propagated to the neighboring nodes appropriate to their velocity, as shown in Fig. 1b-c. The first lattice-gas simulation of a colloidal suspension was programmed in a few weeks, and even with a very rudimentary code, a semi-quantitative calculation of the low-frequency viscosity of a suspension of 100 hard disks was possible.⁽⁷³⁾

The greatest challenge in constructing a lattice-gas model of colloidal suspensions was to devise rules to simulate the hydrodynamic stick boundary conditions at the solid-fluid interfaces. The boundary surface is defined by a set of nodes bordering the perimeter of the solid particle, and the local velocity of each node is determined by the translational and rotational velocities of the solid particle. In ref. 73 the velocity distribution function at the boundary nodes was set to the local equilibrium appropriate to the velocity of the node. However, this distribution neglects velocity gradients and a more accurate boundary condition was clearly necessary. A remarkably simple set of rules, which correctly includes the effects of velocity gradients, was eventually discovered at a workshop devoted to applications of cellular automata.⁽⁷⁴⁾ With these new boundary rules, the friction coefficients between a pair of spheres could be calculated to within 1–2% of the exact result, as long as the gap between the particles was at least one lattice spacing.⁽⁷⁵⁾

Dynamical simulations of a single disk diffusing in a two-dimensional fluid showed that the coupling between statistical fluctuations and hydrodynamics was correctly reproduced. Fig. 2 shows a lattice-gas simulation of the characteristic double vortex pattern of the velocity field around a steadily moving disk. A purely hydrodynamic calculation indicates that the diffusion coefficient of a two-dimensional colloidal particle diverges as $\ln t$, due to the recirculation of the fluid velocity around the particle (Fig. 2).

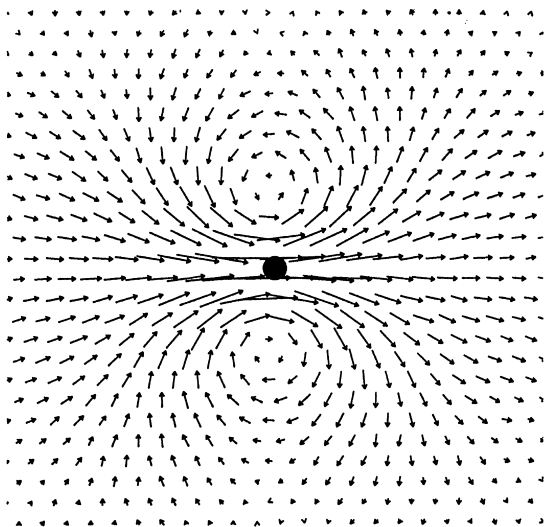


Fig. 2. Lattice-gas simulation of the flow field around a moving disk, showing the double vortex structure of the diffusing momentum field. (Reprinted from ref. 116).

On the other hand, self-consistent mode-coupling theory shows that the strength of the divergence is reduced to $\sqrt{\ln t}$ by particle diffusion from the center of the vortex. Both of these effects have been quantitatively reproduced by lattice-gas simulations.⁽¹¹⁶⁾ Nevertheless, it was eventually realized that the colloidal particles have to be very large with respect to the lattice scale in order to enforce the time-scale separation (Eq. 11) between hydrodynamics and particle diffusion that characterizes real dispersions. The time-scale separation problem was eventually solved with a fluctuating lattice-Boltzmann model,⁽⁶⁸⁾ where the amplitude of the thermal fluctuations could be controlled independently of the particle size.

3. LATTICE-BOLTZMANN METHOD

Lattice-Boltzmann simulations were originally introduced⁽⁹⁰⁾ to simplify the macroscopic dynamics of the lattice-gas model by removing the effects of thermal fluctuations. The averaging inherent in the Boltzmann equation leads to Navier–Stokes dynamics, rather than the fluctuating variant given in Eq. 1. Lattice-Boltzmann simulations of three-dimensional flows typically use linearized collision operators,⁽⁵⁶⁾ which simplify the complex collision rules of three-dimensional lattice gases,⁽³⁰⁾ at the cost of unconditional stability. A crucial advantage of linearized collision operators is that equilibrium distributions can be constructed that lead to

Galilean invariant forms of the hydrodynamic equations.^(23, 89, 104) Further developments in lattice-Boltzmann simulation techniques are summarized in a recent review article.⁽²²⁾

The concepts developed for lattice-gas simulations of colloidal suspensions were readily adapted to the lattice-Boltzmann model.⁽⁶⁹⁾ In particular, the stochastic rules at the solid-fluid boundaries reduce to a deterministic collision operator. The lattice-Boltzmann methodology has been validated by an exhaustive sequence of comparisons with theory, experiment, Stokesian dynamics, and finite-difference methods;⁽⁷⁰⁾ some key results, together with more recent calculations, are summarized in Sections 6 and 7.

The fundamental quantity in the lattice-Boltzmann model is the discretized one-particle velocity distribution function $n_i(\mathbf{r}, t)$, which describes the mass density of particles with velocity \mathbf{c}_i , at a particular node of the lattice \mathbf{r} , at a time t ; \mathbf{r} , t , and \mathbf{c}_i are discrete, whereas n_i is continuous. The hydrodynamic fields, mass density ρ , momentum density $\mathbf{j} = \rho\mathbf{u}$, and momentum flux Π , are moments of this velocity distribution:

$$\rho = \sum_i n_i, \mathbf{j} = \rho\mathbf{u} = \sum_i n_i\mathbf{c}_i, \Pi = \sum_i n_i\mathbf{c}_i\mathbf{c}_i. \quad (12)$$

For simulations of particulate suspensions, the lattice-Boltzmann model has two particularly useful properties. First, the connection to molecular mechanics makes it possible to derive simple local rules for the interactions between the fluid and the suspended solid particles.⁽⁶⁹⁾ Second, the discrete one-particle distribution function, n_i , contains additional information about the dynamics of the fluid beyond that contained in the Navier–Stokes equations; in particular, the fluid stress tensor, although dynamically coupled to the velocity gradient,⁽⁴¹⁾ has an independent significance at short times. This additional flexibility allows us to simulate molecular fluctuations on a mesoscopic scale (see Section 8); *i.e.* length scales of $10^{-6} - 10^{-9}m$ and time scales of $10^{-6} - 10^{-9}s$. To do this, random fluctuations, uncorrelated in space and time, are added to the fluid stress tensor.⁽⁶⁸⁾ Statistical correlations in the particle positions and velocities follow from the hydrodynamic decay of these random fluctuations in fluid stress. This approach is quite different from Brownian dynamics⁽³³⁾ or Stokesian dynamics,⁽¹⁰⁾ where correlated fluctuations are applied directly to the particles.

It is interesting that the lattice-Boltzmann model, with uncorrelated fluctuations in the fluid, contains physics beyond Stokesian dynamics. In Fig. 3, lattice-Boltzmann simulations of the decay of transient translational (U) and rotational (Ω) velocities are compared with the corresponding

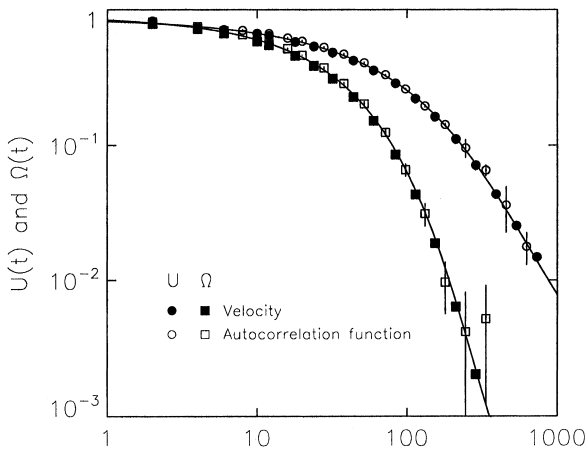


Fig. 3. Decay of the initial velocity (solid symbols) and the decay of the velocity correlation function of an isolated sphere (open symbols with error bars). Lattice Boltzmann simulations are compared with analytic results (solid line).⁽⁵²⁾ (Reprinted from ref. 70).

analytic solutions.⁽⁵²⁾ It can be seen that the lattice-Boltzmann simulations quantitatively reproduce the decay of the particle velocities, including the hydrodynamic memory effects that lead to an algebraic decay at long times. By contrast, Stokes flow hydrodynamics leads to an exponential decay of the particle velocity, which is qualitatively incorrect. Figure 3 also shows the decay of translational and rotational velocity correlation functions in the fluctuating lattice-Boltzmann fluid. The close agreement between the ensemble averaged velocity correlation functions and the decay of initial transients shows that the system obeys the fluctuation-dissipation relation. The time scales required for the temporal development of the hydrodynamic interactions make it computationally demanding to simulate configurational changes in a colloidal suspension by this technique, but such calculations are nevertheless feasible.

Lattice-Boltzmann simulations have also been used to investigate an apparent scaling in the temporal development of hydrodynamic interactions in dense colloidal suspensions. Experimental results from Diffusing Wave Spectroscopy⁽¹²⁵⁾ suggested that velocity correlations in dense suspensions have the same time dependence as a single particle (see Fig. 3), but with a time scale, $\rho a^2/\eta(\phi)$, set by the viscosity of the suspension, rather than the viscosity of the fluid. The surprising observation was that this scaling apparently persisted to very short times, well before viscous momentum diffusion could be expected to establish the collective hydrodynamic interactions described, in a mean-field approximation, by the

suspension viscosity. Initial lattice-Boltzmann simulations obtained a similar scaling,⁽⁶⁸⁾ but more precise simulations⁽⁸²⁾ showed that the scaling is not exact. The deviations from scaling were just too small to be detected within the errors of the earlier experiments and calculations.

Particles larger than a few microns tend to settle out of suspension, due to gravitational forces dominating over the diffusive flux arising from gradients in particle concentration. The detailed dynamics of the most idealized flow, the sedimentation of hard spheres in the absence of inertia and Brownian motion is still controversial. When a suspension sediments, each particle experiences a different shielding of the fluid drag, due to the fluctuating arrangements of its neighbors. These hydrodynamic interactions are long range, decaying asymptotically as $1/R$. They drive large fluctuations in particle velocity, which for particles more than about $10\mu\text{m}$ in diameter completely dominate the thermal Brownian motion. A relatively simple calculation shows that if the particle positions are uncorrelated at large distances, the velocity fluctuations diverge as the container size is increased.⁽¹⁶⁾ It was suggested⁽⁶⁴⁾ that hydrodynamic interactions could be screened by changes in suspension microstructure, analogous to the screening of electrostatic interactions in charged systems. However, lattice-Boltzmann simulations have shown that in a homogeneous suspension (with periodic boundary conditions), particles are distributed randomly at separations beyond a few particle diameters and the velocity fluctuations diverge with increasing container size, in agreement with theory.^(71, 72) Nevertheless, two different sets of experiments have found that the velocity fluctuations converge to a fixed value for sufficiently large systems.^(97, 110) Recent theories have suggested that screening could arise from a convection-diffusion mechanism, coupling hydrodynamic diffusion and density fluctuations to the gravitational field.^(80, 114) On the other hand, it has also been suggested that the container walls may play an important role in the experimental observations.^(15, 84) We have recently carried out a sequence of simulations, with up to 36000 solid particles, to search for changes in suspension microstructure caused by the container walls. In these calculations the velocity fluctuations were observed to saturate with increasing container dimensions, as observed experimentally, but contrary to earlier simulations with periodic boundary conditions. Taken together, the simulation results suggest that saturation may be caused by inhomogeneities introduced by the container walls.⁽⁷⁶⁾

As the particle size increases beyond the colloidal range, fluid inertia can be important. Pressure-driven flows in fixed beds of cylinders⁽⁶³⁾ and spheres⁽⁵⁷⁾ have been investigated by extensive lattice-Boltzmann simulations, at Reynolds numbers up to about 200. One of the interesting discoveries of this work was that a complex sequence of instabilities exists in

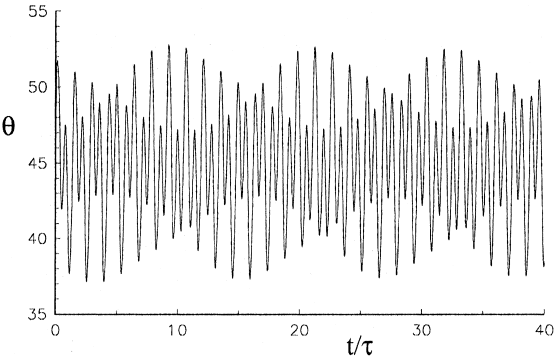


Fig. 4. Temporal variation of the angle of the mean flow θ for the P17 oscillation at $Re = 187$ for a square array of disks. The area fraction is 0.4 and the pressure gradient was directed along the line $x = y$. (Reprinted from ref. 63).

periodic arrays of cylinders and spheres. Although at low Reynolds number the flow in a periodic array is independent of the direction of the pressure gradient, at higher Reynolds numbers, the flow is very sensitive to the orientation of the pressure gradient with respect to the symmetry directions of the lattice. For example, if the pressure gradient is directed along one of the principle axes of a square lattice of cylinders, then, for Reynolds numbers in the range 150-200, a classical period doubling sequence is observed. As the pressure gradient is increased, there are well defined Reynolds numbers where the repeat period doubles. However, if the pressure gradient is oriented at 45° to a principle axis, the initial instability suddenly makes a transition to a sequence of instabilities with a much longer overall repeat period. As an illustration of this work, the angle of the mean flow for a period 17 oscillation is shown in Fig. 4. It can be seen that the lattice-Boltzmann simulation gives a beautiful repeating pattern, with an exact recurrence of the initial state every seventeen periods.

Lattice-Boltzmann methods have also been extended to suspensions of non-spherical particles.⁽¹⁰³⁾ Remarkably, the underlying lattice does not seriously affect the rotation of non-spherical particles. Simulations of the dynamics of disks⁽²⁾ and ellipses⁽¹⁰³⁾ have been compared with finite-element simulations of identical systems.⁽³⁴⁾ These completely independent calculations are in almost exact agreement with one another, which provides a nice validation of both computational methods and their detailed implementations.

4. A 3D LATTICE-BOLTZMANN MODEL

The time evolution of the velocity distribution function, $n_i(\mathbf{r}, t)$, is described by a discrete analogue of the Boltzmann equation,⁽⁴¹⁾

$$n_i(\mathbf{r} + \mathbf{c}_i \Delta t, t + \Delta t) = n_i(\mathbf{r}, t) + \Delta_i[\mathbf{n}(\mathbf{r}, t)], \quad (13)$$

where Δ_i is the change in n_i due to instantaneous molecular collisions at the lattice nodes and Δt is the time step. The time evolution of a lattice-gas is described by a similar equation, except that the continuous population densities are replaced by discrete bit fields. The collision operator $\Delta_i(\mathbf{n})$ depends on all the n_i 's at the node, denoted collectively by $\mathbf{n}(\mathbf{r}, t)$. It can take any form, subject to the constraints of mass and momentum conservation. A computationally useful form for the collision operator can be constructed by linearizing about the local equilibrium \mathbf{n}^{eq} ,⁽⁵⁶⁾ *i.e.*

$$\Delta_i(\mathbf{n}) = \Delta_i(\mathbf{n}^{eq}) + \sum_j \mathcal{L}_{ij} n_j^{neq}, \quad (14)$$

where \mathcal{L}_{ij} are the matrix elements of the linearized collision operator, $n_j^{neq} = n_j - n_j^{eq}$, and $\Delta_i(\mathbf{n}^{eq}) = 0$. The computational utility of lattice-gas and lattice-Boltzmann models depends on the fact that only a small set of velocities are necessary to simulate the Navier-Stokes equations.⁽⁴²⁾

A particular lattice-Boltzmann model is defined by a set of velocities \mathbf{c}_i , an equilibrium distribution n_i^{eq} , and the eigenvalues of the collision operator. The population density associated with each velocity has a weight a^{c_i} that describes the fraction of particles with velocity \mathbf{c}_i in a system at rest; these weights depend only on the speed c_i and are normalized so that $\sum_i a^{c_i} = 1$. Note that the velocities \mathbf{c}_i are chosen such that all particles move from node to node simultaneously. For any cubic lattice,

$$\sum_i a^{c_i} \mathbf{c}_i \mathbf{c}_i = C_2 c^2 \mathbf{1}, \quad (15)$$

where $c = \Delta x / \Delta t$, Δx is the grid spacing, and C_2 is a numerical coefficient that depends on the choice of weights. However, in order for the viscous stresses to be independent of direction, the velocities must also satisfy the isotropy condition;

$$\sum_i a^{c_i} c_{i\alpha} c_{i\beta} c_{i\gamma} c_{i\delta} = C_4 c^4 \{ \delta_{\alpha\beta} \delta_{\gamma\delta} + \delta_{\alpha\gamma} \delta_{\beta\delta} + \delta_{\alpha\delta} \delta_{\beta\gamma} \}. \quad (16)$$

In three dimensions, isotropy requires a multi-speed model; for example the 18-velocity model described in ref. 69. This model uses the [100] and [110] directions of a simple cubic lattice, with twice the density of particles

moving in [100] directions as in [110] directions; alternatively a 14-velocity model can be constructed from the [100] and [111] directions with a density ratio of 7 : 1. Although the 14-velocity model requires less computation and less memory than the 18-velocity model, it suffers from “checkerboard” invariants⁽⁶⁵⁾ and is less accurate. The 18-velocity model can be augmented by stationary particles, which then enables it to account for small deviations from the incompressible limit (Section 5.4), although in simulations of stationary flows we have found the numerical differences to be small. However, the extension to 19 velocities should lead to substantial improvements in the equipartition of energy between particles and fluid in simulations of Brownian suspensions (Section 8.1). In Sections 5 and 8 we present an update of the theory given in ref. 69, to reflect the improvements brought about by including stationary particles. We have not found any additional improvement in accuracy when simulating incompressible flows with a more complex model involving 27 velocities ([000], [100], [110], and [111] directions). However, larger sets of velocities can increase the global stability and are necessary to simulate coupled heat and momentum transport.

4.1. Equilibrium Distribution

The form of the equilibrium distribution is constrained by the moment conditions required to reproduce the inviscid (Euler) equations on large length scales and time scales. In particular, the second moment of the equilibrium distribution should be equal to the inviscid momentum flux $p\mathbf{1} + \rho\mathbf{uu}$:

$$\rho = \sum_i n_i^{eq} \quad (17)$$

$$\mathbf{j} = \sum_i n_i^{eq} \mathbf{c}_i = \rho \mathbf{u} \quad (18)$$

$$\mathbf{\Pi}^{eq} = \sum_i n_i^{eq} \mathbf{c}_i \mathbf{c}_i = \rho c_s^2 \mathbf{1} + \rho \mathbf{uu} \quad (19)$$

The equilibrium distribution can be used in Eqs. 17 and 18 (*c.f.* Eq. 12) because mass and momentum are conserved during the collision process; in other words

$$\sum_i n_i^{neq} = \sum_i n_i^{neq} \mathbf{c}_i = 0. \quad (20)$$

The pressure in Eq. 19, $p = \rho c_s^2$, takes the form of an ideal gas equation of state with adiabatic sound speed c_s . It is also adequate for the liquid phase

if the density fluctuations are small (*i.e.* the Mach number $M = u/c_s \ll 1$), so that $\nabla p = c_s^2 \nabla \rho$.

For small Mach numbers, the equilibrium distribution can be expanded as a power series in $\mathbf{u} \cdot \mathbf{c}_i / c_s^2$, and it then follows from Eq. 19 that the weights must be chosen so that $C_2 = (c_s/c)^2$; *i.e.*

$$\sum_i a^{c_i} \mathbf{c}_i \mathbf{c}_i = c_s^2 \mathbf{1}. \quad (21)$$

A suitable form for the equilibrium distribution of the 19-velocity model that satisfies Eqs. 17–19, as well as the isotropy condition (Eq. 16), is⁽¹⁰⁴⁾

$$n_i^{eq} = a^{c_i} \left[\rho + \frac{\mathbf{j} \cdot \mathbf{c}_i}{c_s^2} + \frac{\rho \mathbf{u} \mathbf{u} : (\mathbf{c}_i \mathbf{c}_i - c_s^2 \mathbf{1})}{2c_s^4} \right], \quad (22)$$

where $c_s = \sqrt{c^2/3}$, and the coefficients of the three speeds are

$$a^0 = \frac{1}{3}, \quad a^1 = \frac{1}{18}, \quad a^{\sqrt{2}} = \frac{1}{36}. \quad (23)$$

In this case the coefficient in Eq. 16 is $C_4 = (c_s/c)^4$.

In contrast to the equilibrium distributions of lattice-gas models,⁽⁴²⁾ Eqs. 22 and 23 ensure that the inviscid hydrodynamic equations are correctly reproduced. The viscous stresses come from moments of the non-equilibrium distribution, as in the Chapman–Enskog solution of the Boltzmann equation. The fundamental limitation of this class of lattice-Boltzmann model is that the Mach number be small, less than 0.3; our suspension simulations always keep $M < 0.1$.

4.2. Collision Operator

The linearized collision operator must satisfy the following eigenvalue equations;

$$\sum_i \mathcal{L}_{ij} = 0, \quad \sum_i \mathbf{c}_i \mathcal{L}_{ij} = 0, \quad \sum_i \overline{\mathbf{c}_i \mathbf{c}_i} \mathcal{L}_{ij} = \lambda \overline{\mathbf{c}_j \mathbf{c}_j}, \quad \sum_i c_i^2 \mathcal{L}_{ij} = \lambda_v c_j^2, \quad (24)$$

where $\overline{\mathbf{c}_i \mathbf{c}_i}$ indicates the traceless part of $\mathbf{c}_i \mathbf{c}_i$. The first two equations follow from conservation of mass and momentum (*c.f.* Eq. 20), and the last two equations describe the isotropic relaxation of the stress tensor; the eigenvalues λ and λ_v are related to the shear and bulk viscosities and lie in the range $-2 < \lambda < 0$. Equation 24 accounts for only 10 of the eigenvectors of \mathcal{L} . The remaining 9 modes are higher-order eigenvectors of \mathcal{L} that are not

relevant to the Navier–Stokes equations, but which do affect the boundary conditions at the solid-fluid interfaces. In general the eigenvalues of these kinetic modes are set to -1 , which both simplifies the simulation and ensures a rapid relaxation of the non-hydrodynamic modes.⁽⁶⁹⁾

In a dilute gas without internal degrees of freedom, energy conservation requires that the eigenvalue of the bulk viscous mode (λ_v in Eq. 24) is zero. Since our model does not include energy conservation, the bulk viscous mode is free to relax, so as to account for all the viscous stresses present in a dense fluid. Alternatively, we can imagine a polyatomic gas where energy can be absorbed into internal degrees of freedom and λ_v is again non-zero.

The collision operator can be further simplified by taking a single eigenvalue for both the viscous and kinetic modes.^(20, 104) This exponential relaxation time (ERT) approximation, $\Delta_i = -n_i^{neq}/\tau$, has become the most popular form for the collision operator because of its simplicity and computational efficiency. However, the absence of a clear time scale separation between the kinetic and hydrodynamic modes can sometimes cause significant errors at solid-fluid boundaries (see Section 6.1), and thus we prefer the more flexible collision operator described by Eq. 24.

In our suspension simulations we use a 3-parameter collision operator, allowing for separate relaxation of the 5 shear modes, 1 bulk mode, and 9 kinetic modes. The post-collision distribution $n_i^\star = n_i + \Delta_i$ is written as a series of moments (Eq. 12), as for the equilibrium distribution (Eq. 22),

$$n_i^\star = a^{c_i} \left(\rho + \frac{\mathbf{j} \cdot \mathbf{c}_i}{c_s^2} + \frac{(\rho \mathbf{u} \mathbf{u} + \Pi^{neq, \star}) : (\mathbf{c}_i \mathbf{c}_i - c_s^2 \mathbf{1})}{2c_s^4} \right). \tag{25}$$

The zeroth (ρ) and first ($\mathbf{j} = \rho \mathbf{u}$) moments are the same as in the equilibrium distribution (Eq. 22), but the non-equilibrium second moment Π^{neq} is modified by the collision process, according to Eq. 24:

$$\Pi^{neq, \star} = (1 + \lambda) \bar{\Pi}^{neq} + \frac{1}{3} (1 + \lambda_v) (\Pi^{neq} : \mathbf{1}) \mathbf{1}, \tag{26}$$

where $\Pi^{neq} = \Pi - \Pi^{eq}$. The kinetic modes can also contribute to the post-collision distribution, but we choose the eigenvalues of these modes to be -1 , so that they have no effect on n_i^\star . Equation 26 with $\lambda = \lambda_v = -1$ is equivalent to the ERT model with $\tau = 1$; for $\lambda < -1$, the kinetic modes relax more rapidly than the viscous modes, which is the proper limit for hydrodynamics.

4.3. External Forces

In the presence of an externally imposed force density \mathbf{f} , for example a pressure gradient or a gravitational field, the time evolution of the lattice-Boltzmann model includes an additional contribution $f_i(\mathbf{r}, t)$,

$$n_i(\mathbf{r} + \mathbf{c}_i \Delta t, t + \Delta t) = n_i(\mathbf{r}, t) + \Delta t [\mathbf{n}(\mathbf{r}, t)] + f_i(\mathbf{r}, t). \quad (27)$$

The forcing term can be expanded in a power series in the particle velocity; *i.e.*

$$f_i = a^{c_i} \left[A + \frac{\mathbf{B} \cdot \mathbf{c}_i}{c_s^2} + \frac{\mathbf{C} : (\mathbf{c}_i \mathbf{c}_i - c_s^2 \mathbf{1})}{2c_s^4} \right] \Delta t, \quad (28)$$

where A , \mathbf{B} , and \mathbf{C} are determined by requiring that the moments of f_i are consistent with the hydrodynamic equations. Then the zeroth and first moments are given by $\sum_i f_i = A = 0$ and $\sum_i f_i \mathbf{c}_i = \mathbf{B} \Delta t = \mathbf{f} \Delta t$ (Eq. 37). The second moment, \mathbf{C} , is usually neglected, but in that case the external force contributes terms of order $\mathbf{u} \mathbf{f} \Delta t$ to the momentum flux (Eq. 40), which do not appear in the macroscopic equations. We describe two ways in which these extraneous terms can be accounted for. If these terms are cancelled by taking $\mathbf{C} = \mathbf{u} \mathbf{f} + \mathbf{f} \mathbf{u}$,⁽⁸⁵⁾ a multi-scale expansion (Section 5) shows that a different definition of the momentum density is required (see Section 5.3), namely

$$\mathbf{j}' = \rho \mathbf{u}' = \sum_i n_i \mathbf{c}_i + \frac{\Delta t}{2} \mathbf{f}. \quad (29)$$

However, if the conventional definition of the momentum flux (Eq. 12) is retained, the expression for \mathbf{C} must be modified to account for discrete lattice effects (Eq. 47). Nevertheless, for a spatially uniform force, numerical simulations show that variations in \mathbf{C} have a negligible effect on the flow.

4.4. Stationary Flows

At low Reynolds numbers, the evolution of a time-independent flow field can be extremely slow, especially in systems of very high porosity (*i.e.* dilute suspensions) or very low porosity (*i.e.* porous rocks). In such circumstances the lattice-Boltzmann method typically requires $10^4 - 10^5$ cycles to reach steady state. However, a new numerical method has been developed⁽¹²⁰⁾ to directly simulate the equations for Stokes flow (Eq. 9). The method is based on the lattice-Boltzmann approach, but utilizes an implicit

solution of time-independent equations, rather than the usual temporal evolution to steady state.

For low Reynolds numbers, a simplified form for the equilibrium distribution can be used, ignoring terms in $\rho \mathbf{u} \mathbf{u}$,⁽⁶⁹⁾

$$n_i^{eq} = a^{c_i} \left(\rho + \frac{\mathbf{j} \cdot \mathbf{c}_i}{c_s^2} \right). \tag{30}$$

Setting the viscous eigenvalues $\lambda = \lambda_v = -1$, the update of the lattice-Boltzmann equation can be rewritten in terms of the mass and momentum densities at each node:

$$\begin{aligned} n_i(\mathbf{r} + \mathbf{c}_i \Delta t, t + \Delta t) &= n_i^{eq}(\mathbf{r}, t) + f_i(\mathbf{r}, t) \\ &= a^{c_i} \left(\rho(\mathbf{r}, t) + \frac{[\mathbf{j}(\mathbf{r}, t) + \mathbf{f}(\mathbf{r}, t) \Delta t] \cdot \mathbf{c}_i}{c_s^2} \right), \end{aligned} \tag{31}$$

where the non-linear forcing can be ignored ($Re = 0$). Taking moments of Eq. 31, linear equations for the time evolution of the mass and momentum densities are obtained. At steady state $n_i(\mathbf{r}, t + \Delta t) = n_i(\mathbf{r}, t)$, and the resulting linear system of equations can be efficiently solved with the bi-conjugate gradient method.⁽⁴⁸⁾ It should be noted that this linear system is under-determined, since the velocity boundary conditions do not set the mean mass density in the system. The total mass, which is usually an initial condition, has to be included as an additional constraint.² With careful programming, the new algorithm requires about 50% more memory and computational time per cycle than the conventional lattice-Boltzmann model, but reduces the number of cycles by up to two orders of magnitude at the extremes of porosity (low and high). The computational speed can perhaps be further improved by pre-conditioning the coefficient matrix.

5. MACROSCOPIC DYNAMICS

The macrodynamical behavior arising from the lattice-Boltzmann equation can be found from a multi-time-scale analysis,⁽⁴¹⁾ using an expansion parameter ϵ , defined as the ratio of the lattice spacing to a characteristic macroscopic length; the hydrodynamic limit corresponds to $\epsilon \ll 1$.

² In ref. 120 we stated that the time-independent equations for the distribution function are under-determined and can only be solved by projecting onto the mass and momentum densities. However, we have since discovered that this is incorrect, and that the stationary distribution function can be solved for directly, once the mass constraint is included. Nevertheless, the method described in ref. 120 is much more efficient computationally, since it involves only 4 variables per node rather than 18 or 19.

Exact conservation equations for the moments of the distribution function can be derived from Eq. 27:

$$\begin{aligned} \sum_i n_i(\mathbf{r} + \mathbf{c}_i \Delta t, t + \Delta t) \mathbf{c}_i^n \\ = \sum_i n_i(\mathbf{r}, t) \mathbf{c}_i^n + \sum_i \sum_j \mathcal{L}_{ij} n_j^{neq}(\mathbf{r}, t) \mathbf{c}_i^n + \sum_i f_i(\mathbf{r}, t) \mathbf{c}_i^n. \end{aligned} \quad (32)$$

where \mathbf{c}_i^n represents a tensor of rank n , comprising the outer products of vectors \mathbf{c}_i . The scaling parameter ϵ plays a similar role to the Knudsen number in the Chapman–Enskog method,⁽¹⁸⁾ separating the relaxation of equilibrium and non-equilibrium distributions;

$$n_i = n_i^{eq} + \epsilon n_i^1, \quad (33)$$

where $n_i^{neq} = \epsilon n_i^1$. However, because the lattice spacing and the mean-free path are comparable, there are additional contributions to the viscous momentum flux, which do not appear in the ordinary kinetic theory of gases. In order to remove discrete lattice artifacts from the macroscopic equations, a macroscopic space scale $\mathbf{r}_1 = \epsilon \mathbf{r}$ is defined, together with two macroscopic time scales $t_1 = \epsilon t$ and $t_2 = \epsilon^2 t$. The propagation of sound (t_1 time scale), which involves first-order spatial derivatives, is then mathematically separated from the diffusion of vorticity (t_2 time scale), which involves second-order spatial derivatives.⁽⁴¹⁾ The external force density enters the multi-scale expansion at order ϵ .

5.1. First-Order Expansion

Expanding the finite differences, $n_i(\mathbf{r} + \mathbf{c}_i \Delta t, t + \Delta t) - n_i(\mathbf{r}, t)$, in Eq. 32 about \mathbf{r} and t , and collecting terms that are first order in ϵ , we obtain the relaxation of the moments of n_i on the t_1 time scale:

$$\partial_{t_1} \rho + \nabla_1 \cdot (\rho \mathbf{u}) = A_1, \quad (34)$$

$$\partial_{t_1} (\rho \mathbf{u}) + \nabla_1 \cdot (\rho c_s^2 \mathbf{1} + \rho \mathbf{u} \mathbf{u}) = \mathbf{B}_1, \quad (35)$$

$$\begin{aligned} \partial_{t_1} (\rho c_s^2 \mathbf{1} + \rho \mathbf{u} \mathbf{u}) + \nabla_1 \cdot \sum_i n_i^{eq} \mathbf{c}_i \mathbf{c}_i \\ = \frac{\lambda}{\Delta t} \bar{\Pi}_1 + \frac{\lambda_v}{3 \Delta t} (\Pi_1 : \mathbf{1}) \mathbf{1} + A_1 c_s^2 \mathbf{1} + \mathbf{C}_1, \end{aligned} \quad (36)$$

where the first-order momentum flux $\Pi_1 = \sum_i n_i^1 c_{i\alpha} c_{i\beta} = \epsilon^{-1} \Pi^{neq}$, and $A = \epsilon A_1$, $\mathbf{B} = \epsilon \mathbf{B}_1$, and $\mathbf{C} = \epsilon \mathbf{C}_1$ are the coefficients in Eq. 28. The gradient operator refers to derivatives on the macroscopic space scale \mathbf{r}_1 , *i.e.*

$\nabla_1 \equiv \partial_{r_1}$. To recover the Euler equations from Eqs. 34 and 35, the first two coefficients in Eq. 28 must be

$$A = 0, \quad \mathbf{B} = \mathbf{f}. \quad (37)$$

Equation 36 can be simplified by using Eqs. 34 and 35 to express the time derivatives of ρ and $\rho\mathbf{u}$ in terms of spatial derivatives,

$$\begin{aligned} \partial_{t_1}(\rho c_s^2 \mathbf{1} + \rho \mathbf{u} \mathbf{u}) \\ = -c_s^2 [(\mathbf{u} \nabla_1 \rho) + (\mathbf{u} \nabla_1 \rho)^\dagger + (\nabla_1 \cdot \rho \mathbf{u}) \mathbf{1}] + \mathbf{u} \mathbf{B}_1 + \mathbf{B}_1 \mathbf{u} + \mathcal{O}(u^3), \end{aligned} \quad (38)$$

and evaluating the spatial derivative of the third-order moment directly from Eqs. 22 and 23,

$$\nabla_1 \cdot \sum_i n^{eq} \mathbf{c}_i \mathbf{c}_i \mathbf{c}_i = c_s^2 [(\nabla_1 \rho \mathbf{u}) + (\nabla_1 \rho \mathbf{u})^\dagger + (\nabla_1 \cdot \rho \mathbf{u}) \mathbf{1}]. \quad (39)$$

The error term in Eq. 38 is of order $u^2/c_s^2 = M^2$ in comparison to the leading order terms, and can be neglected for incompressible or nearly incompressible flows. Combining these results with Eq. 36, the momentum flux on the t_1 time scale is given by

$$\begin{aligned} \frac{\lambda}{\Delta t} \bar{\Pi}_1 + \frac{\lambda_v}{3\Delta t} (\Pi_1 : \mathbf{1}) \mathbf{1} \\ = \rho c_s^2 [(\nabla_1 \mathbf{u}) + (\nabla_1 \mathbf{u})^\dagger] + \mathbf{u} \mathbf{B}_1 + \mathbf{B}_1 \mathbf{u} - \mathbf{C}_1 + \mathcal{O}(u^3). \end{aligned} \quad (40)$$

Equation 40 can be rearranged to give the momentum flux Π_1 in terms of velocity gradients and external forces,

$$\Pi_1 = -\sigma_1^c + \frac{\Delta t}{\lambda} [\overline{\mathbf{u} \mathbf{B}_1} + \overline{\mathbf{B}_1 \mathbf{u}} - \overline{\mathbf{C}_1}] + \frac{\Delta t}{3\lambda_v} [2\mathbf{u} \cdot \mathbf{B}_1 - \mathbf{C}_1 : \mathbf{1}] \mathbf{1}. \quad (41)$$

The collisional stress tensor, σ_1^c , has the form of the Navier–Stokes stress (*c.f.* Eq. 3),

$$\sigma_1^c = \eta^c [(\nabla_1 \mathbf{u}) + (\nabla_1 \mathbf{u})^\dagger] - \frac{2}{3} (\nabla_1 \cdot \mathbf{u}) \mathbf{1} + \eta_v^c (\nabla_1 \cdot \mathbf{u}) \mathbf{1}. \quad (42)$$

with independent shear and bulk viscosities:

$$\eta^c = -\rho c_s^2 \Delta t \frac{1}{\lambda}, \quad \eta_v^c = -\rho c_s^2 \Delta t \frac{2}{3\lambda_v}. \quad (43)$$

If the coefficient of the forcing is taken to be $\mathbf{C} = \mathbf{u}\mathbf{f} + \mathbf{f}\mathbf{u}$, then the momentum flux reduces to the Navier–Stokes expression for the viscous stresses, $\Pi_1 = -\sigma_1^c$. This is the expression for \mathbf{C} given in ref. 85 and is the same as in the Chapman–Enskog solution of the Boltzmann equation. However, for the lattice-Boltzmann equation, there are additional contributions to the viscous stresses, which modify the viscosities and the forcing. These corrections can be found from the second-order terms in the ϵ -expansion, using the expression for the momentum flux (Eq. 41) where \mathbf{C} remains undetermined.

5.2. Second-Order Expansion

The t_2 relaxation of the mass and momentum densities can be found from the order ϵ^2 terms in the expansion of Eq. 32:

$$\partial_{t_2}\rho + \frac{\Delta t}{2} \nabla_1 \cdot \mathbf{B}_1 = 0, \quad (44)$$

$$\begin{aligned} \partial_{t_2}(\rho\mathbf{u}) + \frac{\Delta t}{2} \nabla_1 \cdot [\rho c_s^2(\nabla_1\mathbf{u}) + \rho c_s^2(\nabla_1\mathbf{u})^\dagger + \mathbf{u}\mathbf{B}_1 + \mathbf{B}_1\mathbf{u}] \\ = \nabla_1 \cdot \sigma_1^c - \frac{\Delta t}{\lambda} \nabla_1 \cdot [\overline{\mathbf{u}\mathbf{B}_1} + \overline{\mathbf{B}_1\mathbf{u}} - \overline{\mathbf{C}_1}] - \frac{\Delta t}{3\lambda_v} \nabla_1 \cdot [2\mathbf{u} \cdot \mathbf{B}_1 - \mathbf{C}_1 : \mathbf{1}] \mathbf{1} \\ - \frac{\Delta t}{2} \partial_{t_1}\mathbf{B}_1 + \mathcal{O}(u^3). \end{aligned} \quad (45)$$

In this section it will be assumed that any external forcing is time independent, so that $\partial_{t_1}\mathbf{B}_1 = 0$. In the absence of external forcing, the fluid is incompressible on the t_2 time scale (Eq. 44); all density fluctuations decay on the t_1 time scale by propagation of sound waves. If the force density is uniform, the fluid is still incompressible on the t_2 time scale, but if \mathbf{f} is spatially varying, density fluctuations relax more slowly and may interfere with the viscous momentum diffusion. However, if the external force is a gravitational field, so that $\mathbf{f} = \rho\mathbf{g}$ with \mathbf{g} a uniform gravitational acceleration, the fluid remains incompressible for low Mach number flows ($\nabla\rho \approx \mathcal{O}(M^2)$: *c.f.* Eq. 57).

The terms in square brackets on the left hand side of Eq. 45 are an artifact of the discrete lattice and do not appear in the continuous Boltzmann equation. However, the first two terms can be absorbed into the definition of the viscous stress, σ_1 , analogous to Eq. 42, but with an additional lattice contribution to the shear and bulk viscosities (*c.f.* Eq. 43):

$$\eta = -\rho c_s^2 \Delta t \left(\frac{1}{\lambda} + \frac{1}{2} \right), \quad \eta_v = -\rho c_s^2 \Delta t \left(\frac{2}{3\lambda_v} + \frac{1}{3} \right). \quad (46)$$

These lattice contributions to the viscosity have been known for a long time, but in order to remove all traces of the external force from the t_2 momentum relaxation we must also include the lattice contribution to the forcing, proportional to $\mathbf{u}\mathbf{f}$ as suggested in ref. 85, but with a coefficient given by

$$\mathbf{C} = \frac{1}{2} (2 + \lambda)(\overline{\mathbf{u}\mathbf{f}} + \overline{\mathbf{f}\mathbf{u}}) + \frac{1}{3} (2 + \lambda_v)(\mathbf{u} \cdot \mathbf{f}) \mathbf{1}. \tag{47}$$

Then the momentum diffusion can be written in Navier–Stokes form

$$\partial_{t_2}(\rho\mathbf{u}) = \nabla_1 \cdot \boldsymbol{\sigma}_1 + \mathcal{O}(u^3), \tag{48}$$

with relative errors of order M^2 .

The shear and bulk viscosities characterizing $\boldsymbol{\sigma}_1$ can be adjusted by varying the eigenvalues λ and λ_v (Eq. 46), but a linear stability analysis shows that eigenvalues must be bounded in the range $-2 < \lambda < 0$.^(56, 89) The bounds on λ and λ_v correspond to the simple physical requirement that the viscosities are positive. For a particular choice of viscosity, there is a unique definition of the forcing (Eqs. 28, 37, and 47) that removes all lattice artifacts from the momentum equation to order u^3 .

For a complete error analysis, the multi-scale expansion must be extended to order ϵ^3 . Although explicit calculations are rather lengthy, it can be shown that both $\partial_{t_3}\rho$ and $\partial_{t_3}(\rho\mathbf{u})$ are of order u^2 . Thus the largest error terms are of order ϵ^2u^3 and ϵ^3u^2 ; the fourth-order terms in the multi-scale expansion are at least order ϵ^4 and most likely ϵ^4u . Convective flows are of order ϵu and diffusive flows are of order ϵ^2u , so that for sufficiently low velocities the convergence is quadratic in the lattice spacing. The Navier–Stokes equations are recovered by combining the relaxation of the mass and momentum densities on the t_1 and t_2 time scales ($\partial_t = \epsilon\partial_{t_1} + \epsilon^2\partial_{t_2}$, $\nabla = \epsilon\nabla_1$):

$$\begin{aligned} \partial_t \rho + \nabla \cdot (\rho\mathbf{u}) &= 0 \\ \partial_t(\rho\mathbf{u}) + \nabla \cdot (\rho\mathbf{u}\mathbf{u}) + \nabla \rho c_s^2 &= \mathbf{f} + \nabla \cdot \boldsymbol{\sigma}, \end{aligned} \tag{49}$$

where the stress tensor is given by Eq. 3 and the viscosities by Eq. 46.

5.3. Modified Momentum Density

It was shown in the previous section (5.2) that the usual definition of the momentum density (Eq. 12) requires an external force density that involves the eigenvalues of the viscous stress tensor (Eq. 47). Here we show that a simpler and more flexible result is possible, using a redefinition of the momentum density that includes the external force density (Eq. 29).

Moreover, this new definition of the momentum density is more consistent with results obtained using constant velocity boundary conditions than the normal definition of the momentum density⁽⁷⁰⁾ (see Section 6).

The continuity equation obtained from the t_1 (Eq. 34) and t_2 (Eq. 44) timescales contains a term proportional to \mathbf{f} ,

$$\partial_t \rho + \nabla \cdot (\rho \mathbf{u}) + \frac{\Delta t}{2} \nabla \cdot \mathbf{f} = 0, \quad (50)$$

which we have previously argued is small if the system is in a uniform gravitational field (see Section 5.2). Nevertheless, with the modified definition of the velocity field (*c.f.* Eq. 29),

$$\mathbf{u}' = \mathbf{u} + \frac{\Delta t}{2} \mathbf{g}, \quad (51)$$

the exact continuity equation is obtained,⁽⁴⁵⁾

$$\partial_t \rho + \nabla \cdot (\rho \mathbf{u}') = 0, \quad (52)$$

even for spatially varying force densities or accelerations ($\mathbf{f} = \rho \mathbf{g}$).

The coefficient \mathbf{C} in the external force density is taken to be $\mathbf{C} = \mathbf{u}\mathbf{f} + \mathbf{f}\mathbf{u}$, as in the continuous Boltzmann equation, and the t_2 evolution of the momentum density can then be written as (*c.f.* Eqs. 45),

$$\partial_{t_2}(\rho \mathbf{u}) + \frac{\Delta t}{2} \partial_{t_1} \mathbf{B}_1 + \frac{\Delta t}{2} \nabla_1 \cdot [\mathbf{u} \mathbf{B}_1 + \mathbf{B}_1 \mathbf{u}] = \nabla_1 \cdot \boldsymbol{\sigma}_1 + \mathcal{O}(u^3). \quad (53)$$

The combined equation for the momentum density follows by ignoring terms of order ϵ^3 and higher;

$$\partial_t(\rho \mathbf{u}') + \nabla \cdot (\rho \mathbf{u}' \mathbf{u}') + \nabla \rho c_s^2 = \mathbf{f} + \nabla \cdot \boldsymbol{\sigma}', \quad (54)$$

where $\boldsymbol{\sigma}'$ indicates that the modified velocity field is used. In obtaining this equation we have ignored a convective term of order $\Delta t^2 \nabla \cdot \rho \mathbf{g} \mathbf{g}$ and viscous terms of order $\Delta t \nabla \rho \nabla \mathbf{g}$, both of which are of order ϵ^3 . The first term is also proportional to u^2 and thus is the same order as other error terms. The second term is only proportional to u and so introduces a larger error when \mathbf{g} is spatially varying, but for a uniform external field the second term vanishes.

5.4. Limiting Cases

The viscosity in the lattice-Boltzmann model is not independent of density as expected from kinetic theory, but has a linear density depen-

dence, $\eta \propto \rho$; the reason is that the lattice-Boltzmann collision rate is independent of density rather than inversely proportional to density as it is for a dilute gas. However, under most circumstances of physical interest the effects of this discrepancy are negligible.

At low Mach numbers, the Navier–Stokes equations can be re-scaled to the equations of incompressible fluid flow. Using a characteristic length scale, L , and fluid velocity, U , the re-scaled equations are

$$\begin{aligned} \partial_t \rho + \nabla \cdot (\rho \mathbf{u}) &= 0 \\ \partial_t (\rho \mathbf{u}) + \nabla \cdot (\rho \mathbf{u} \mathbf{u}) + \frac{1}{M^2} \nabla \rho &= \frac{1}{UL} \nabla \cdot \boldsymbol{\sigma}. \end{aligned} \tag{55}$$

Expanding the density and velocity in powers of $M = U/c_s$ about the incompressible limit ρ_0 and \mathbf{u}_0 (ρ_0 is constant)⁽⁸⁶⁾

$$\begin{aligned} \rho &= \rho_0 (1 + M \rho'_1 + M^2 \rho'_2 \dots) \\ \mathbf{u} &= \mathbf{u}_0 + M \mathbf{u}_1 + M^2 \mathbf{u}_2 \dots, \end{aligned} \tag{56}$$

it follows that $\rho'_1 = 0$, and thus the density variations are of order M^2 . At order M^0 we obtain the incompressible fluid equations

$$\begin{aligned} \nabla \cdot \mathbf{u}_0 &= 0 \\ \partial_t \mathbf{u}_0 + \mathbf{u}_0 \cdot \nabla \mathbf{u}_0 + \nabla \rho'_2 &= \frac{1}{Re} \nabla^2 \mathbf{u}_0, \end{aligned} \tag{57}$$

with deviations of order M^2 . The pressure variations in an incompressible fluid are equivalent to the second order variations in density ($\nabla \rho_2$) in the low Mach number limit. Lattice-Boltzmann simulations of the incompressible Navier–Stokes equations have been validated by detailed comparisons with finite-difference and spectral methods,^(23, 88, 89) a review of this work can be found in ref. 22.

The incompressible limit is appropriate to most macroscopic flows. However the decay of spontaneous thermal fluctuations takes place on shorter time scales $t \approx L/c_s \ll L/U$. In this case, it can no longer be assumed that the density fluctuations are negligible, so Eq. 57 no longer applies. However, since the fluctuations are small, it is legitimate to linearize the equations to small variations about equilibrium, $\rho = \rho_0$, $\mathbf{u} = 0$.⁽⁴¹⁾

$$\begin{aligned} \partial_t \rho' + \nabla \cdot \mathbf{u} &= 0 \\ \partial_t \mathbf{u} + c_s^2 \nabla \rho' &= \nu \nabla^2 \mathbf{u} + (\nu_l - \nu) \nabla (\nabla \cdot \mathbf{u}), \end{aligned} \tag{58}$$

where $\rho' = \rho/\rho_0$, $v = \eta/\rho$, and $v_l = (\frac{4}{3}\eta + \eta_v)/\rho$. Again the spatial variation of the transport coefficients can be ignored. It is possible to derive lattice-Boltzmann models that are incompressible on the t_1 time scale,⁽⁵³⁾ but the behavior of these models in response to random thermal fluctuations is not yet known.

6. SOLID-FLUID BOUNDARY CONDITIONS

To simulate the hydrodynamic interactions between solid particles in suspension, the lattice-Boltzmann model must be modified to incorporate the boundary conditions imposed on the fluid by the solid particles. Stationary solid objects were first introduced into lattice-gas simulations by replacing the normal collision rules at a specified set of boundary nodes by the “bounce-back” collision rule,⁽⁴¹⁾ in which incoming particles are reflected back towards the nodes they came from. Surface forces are calculated from the momentum transfer at each boundary node and summed to give the force and torque on each object.⁽⁶⁹⁾ In contrast to finite-difference and finite-element methods, where local surface normals are required to integrate the stresses over the particle surface, the bounce-back rule eliminates these complications by directly summing the surface forces.

6.1. Bounce-Back Rules

Theoretical analysis of the bounce-back rule for two-dimensional channel flow has shown that the location of the zero-velocity plane is shifted from the location of the boundary nodes, into the fluid, by an amount $\Delta = 0.5\Delta x + \mathcal{O}(L^{-1})$,^(27, 45) where L is the channel width. For plane surfaces, the solution can be interpreted in terms of a hydrodynamic boundary displaced into the fluid by half a lattice spacing from the physical one.⁽¹²⁶⁾ An alternative to the “nodal bounce-back” rule is to place the boundary nodes midway between interior (solid) and exterior (fluid) nodes.^(74, 113) The normal collision rules are carried out at all fluid nodes, and augmented by bounce-back rules at the midpoints of links connecting lattice nodes on either side of the particle surface. In this case it can be shown⁽⁵⁴⁾ that the hydrodynamic boundary is now located at the boundary nodes (*i.e.* midway between lattice nodes), again with deviations of order L^{-1} . In Poiseuille flow both the “link bounce-back” and the “displaced nodal bounce-back” rules give velocity fields that deviate from the exact solution by a constant slip velocity, $u_s = u_{LBE} - u_{Exact}$, proportional to L^{-2} ,⁽⁵⁴⁾

$$u_s/u_c = \beta \Delta x^2/L^2, \quad (59)$$

where $u_c = L^2 |\nabla p|/8\nu$ is the exact velocity at the center of the channel and the coefficient β depends on the eigenvalues of the collision operator. However, the nodal bounce-back and link bounce-back rules can be significantly different if the solid surface is moving with respect to the fluid (see the end of Section 7.1).

For the ERT model with non-dimensional relaxation time $\tau = -\lambda^{-1}$,⁽⁵⁴⁾

$$\beta = \frac{1}{3} (16\tau^2 - 20\tau + 3), \tag{60}$$

whereas for the linear collision operator in ref. 69

$$\beta = \frac{1}{3} (4\tau - 5). \tag{61}$$

The displacement, Δ , of the hydrodynamic boundary from the physical boundary can be expressed in terms of β ; for small displacements, $\Delta = -\beta \Delta x^2/4L$. Thus, the bounce-back rule leads to a 2nd-order accurate velocity field, although the location of the hydrodynamic boundary is only first-order. The hydrodynamic boundary and the physical boundary are coincident for sufficiently wide channels, whereas if the velocity field were only first-order accurate, the displacement of the hydrodynamic boundary would tend to a constant for large L .

For small viscosities (*i.e.* $\tau \rightarrow \frac{1}{2}$) $\beta \rightarrow -1$, independent of collision model, but for $\tau > 1$ the ERT slip velocity is sensitive to viscosity and diverges as τ^2 for large τ (Eq. 60). However, for collision operators that include a time-scale separation between the kinetic and hydrodynamic modes (see Section 4.2, Eq. 24), the slip velocity diverges only linearly with τ (Eq. 61), and for $\tau > 2$ is at least an order of magnitude smaller than in the ERT model.⁽⁴³⁾

In the presence of an external force density $\mathbf{f} = -\nabla p$, a further complication arises from the discrete time step of the lattice-Boltzmann model (Eq. 27). In most published work, the velocity field $\rho \mathbf{u} = \sum_i n_i \mathbf{c}_i$ is measured before the application of the force density, but it could equally well be measured afterwards. The velocity fields before (\mathbf{u}) and after (\mathbf{u}_+) applying the force density are related,

$$\rho \mathbf{u}_+ = \rho \mathbf{u} + \mathbf{f} \Delta t. \tag{62}$$

Thus the slip velocities defined in Eqs. 60 and 61 depend on when the velocity field is measured. To decide on the correct choice for the definition of the velocity field, we can compare results obtained with an external pressure gradient with those obtained with another method of driving the fluid flow. In ref. 70, pressure-driven flow past a periodic arrays of spheres

was compared with a constant velocity boundary condition. In the latter case, a quasi-periodic system, with several unit cells in the flow direction, was used to obtain the proper inlet and outlet boundary conditions at the central cell. The mean flow velocity and drag force were measured for this central cell only; different numbers of cells were taken to ensure that there were no artifacts introduced by the boundary conditions at the ends of the system. The results for quasi-periodic systems agreed exactly with results obtained with a pressure gradient, *if* the mean of the velocity field before and after forcing, $\mathbf{u}' = (\mathbf{u}_+ + \mathbf{u})/2$, was used.⁽⁷⁰⁾ Moreover, this definition of the momentum density is also consistent with the Navier–Stokes equations (Section 5.3). The corrected slip velocities from Eqs. 60 and 61 are therefore

$$\beta = \frac{1}{3} (16\tau^2 - 16\tau + 1) \quad (63)$$

for the ERT model, and

$$\beta = \frac{1}{3} (8\tau - 7) \quad (64)$$

for the linear collision operator in ref. 69. We note that boundary conditions that have been tuned to give $\mathbf{u} = 0$ at the solid-fluid interface⁽⁵⁴⁾ are no longer exact if we take the velocity field

$$\rho\mathbf{u}' = \rho\mathbf{u} + \frac{1}{2}\mathbf{f}\Delta t. \quad (65)$$

The velocity field in a channel flow is not very sensitive to the definition of the fluid velocity, but the differences are significant in a low porosity medium, where the velocity field at the same pressure gradient is much smaller. As further evidence that the velocity field should be measured in the middle of the forcing step (Eq. 65), startup flows in a two-dimensional channel have been simulated and compared with analytic results. At $t = 0$ a uniform pressure gradient was applied and the velocity in the channel was compared with the exact solution as a function of time. The coefficient $\beta_{RMS}(t)$ characterizing the time-dependent slip velocity (*c.f.* Eq. 59),

$$\beta_{RMS}(t) = \left(\frac{L}{\Delta x} \right)^{3/2} \left(\frac{\sum_y [u_{LBE}(y, t) - u_{Exact}(y, t)]^2}{u_{Exact}^2(L/2, t)} \right)^{1/2} \quad (66)$$

is shown in Fig. 5 for the different velocity measurements. The root-mean-square error in the velocity field, relative to the velocity at the centerline, is $\beta_{RMS}\Delta x^2/L^2$, and for stationary flows, β_{RMS} is equivalent to the slip coefficient β defined in Eq. 59. In each case we have chosen the viscosity of the fluid such that the slip velocity vanishes at steady state; for velocity fields

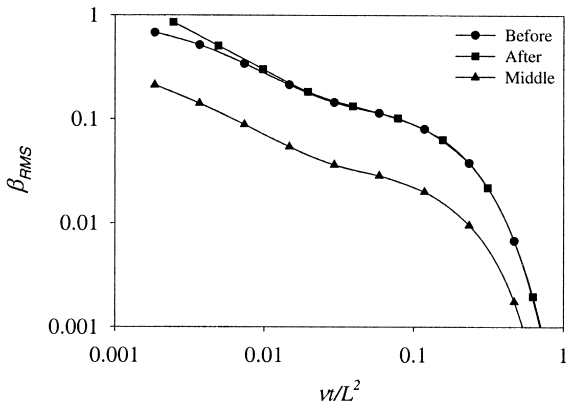


Fig. 5. Startup of a pressure driven flow in a two-dimensional channel. Errors in lattice-Boltzmann results are derived by comparison with the exact solution.

measured before, after, and in the middle of the forcing, the relaxation times were $\tau = \frac{5}{4}$, $\tau = \frac{3}{4}$, and $\tau = \frac{7}{8}$ respectively. During startup, the error in the velocity field is a factor of 4 smaller when it is measured after half the force has been applied (Eq. 65) than in the other two cases.

6.2. Link-Bounce-Back Rules for Particles

The link-bounce-back boundary condition is straightforward to implement, even for non-planar surfaces. Solid particles are defined by a boundary surface, which can be any size or shape; in Fig. 6 it is a circle. The boundary surface cuts some of the links between lattice nodes, and fluid particles moving along these links interact with the solid surface at boundary nodes placed halfway along the links. Thus we obtain a discrete representation of the particle surface, which becomes more and more precise as the particle gets larger. Lattice nodes on either side of the boundary surface are treated in an identical fashion, so that fluid fills the whole volume of space, both inside and outside the solid particles. However, because of the relatively small volume inside each particle, the interior fluid quickly relaxes to rigid-body motion, characterized by the particle velocity and angular velocity. For stationary particles the interior fluid is at rest and can be ignored.

Although the link-bounce-back rule is second order accurate for planar walls oriented along lattice symmetry directions, it is only first order for channels oriented at arbitrary angles.^(45, 46) Thus for large channels, the hydrodynamic boundary is displaced by an amount Δ from the physical

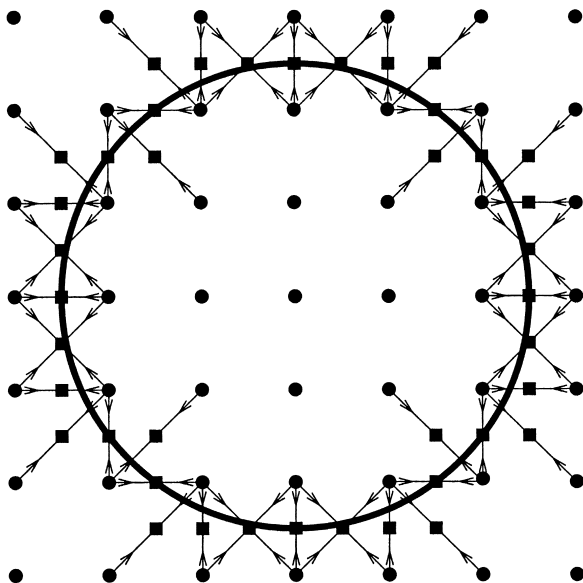


Fig. 6. Location of the boundary nodes for a circular object of radius 2.5 lattice spacings. The velocities along links cutting the boundary surface are indicated by arrows. The locations of the boundary nodes are shown by solid squares and the lattice nodes by solid circles. (Figure reprinted from ref. 69).

boundary, where Δ is independent of L but depends on the orientation of the channel. However, second-order convergence can be recovered by taking the channel width as $L - 2\Delta$, rather than L . Convex bodies sample a variety of boundary orientations, so that it is not possible to make an analytical determination of the displacement of the hydrodynamic boundary from the solid particle surface. Nevertheless, the displacement of the boundary can be determined numerically from simulations of flow around isolated particles. By considering the size of the particles to be the hydrodynamic radius, $a + \Delta$, rather than the physical radius a , approximate second-order convergence can be obtained for dense suspensions.⁽⁷⁰⁾

Numerical calculations have shown that for relaxation times close to unity, the displacement of the boundary surface is small, less than $0.05\Delta x$. However to simulate flow at non-zero Reynolds numbers, it is often necessary to reduce the viscosity in order to keep the Mach number small. In a study of inertial flow in periodic and random arrays of cylinders⁽⁶³⁾, a kinematic shear viscosity of $0.01\Delta x^2/\Delta t$ ($\tau = 0.53$) was used, giving an upper limit to the Reynolds number of approximately $5L/\Delta x$ (with $M < 0.1$), where L is the characteristic spatial dimension. For particles larger than about $5\Delta x$ the hydrodynamic boundary is displaced into the

fluid by a constant amount $\Delta = 0.3\Delta x$. For smaller particles there are additional deviations, since the physical size itself is not uniquely defined.

It has been shown⁽⁷⁰⁾ that the hydrodynamic radius depends only on particle size and fluid viscosity, but not on the particle configuration, flow geometry or Reynolds number. Thus, it is a well-defined physical parameter that can be determined by a single calibration experiment. Fluid flow through a periodic array of cylinders has been used for both calibration, and as a test of the effectiveness of the bounce-back rule in a typical suspension geometry. The present calculations are an extension of published work⁽⁷⁰⁾ to include simulations with a 1000-fold variation in fluid viscosity. Cylinders of nominal radius 2.5, 7.5, 22.5, and 67.5 lattice units have been used to simulate flow at an area fraction of approximately 40%; the ratio of the drag force to the mean flow velocity was compared with essentially exact results,⁽¹⁰⁷⁾ as described in ref. 70. The drag force at this density is large, $F_D \approx 220\eta U$, so this calculation is a severe test of the method.

The relative errors shown in Fig. 7 are based on the nominal radius of the disk (left) and on the hydrodynamic radius (right), which was obtained by fitting the measured drag coefficient at an area fraction of 10%. If the comparisons with ref. 107 are based on the nominal radius of the disk, approximately linear convergence with increasing resolution is observed. From the previous discussion it is clear that the hydrodynamic boundary has been displaced from the physical one, which is determined by the location of the boundary nodes. The displacement of the boundary is particularly severe when the relaxation time deviates significantly from unity. For

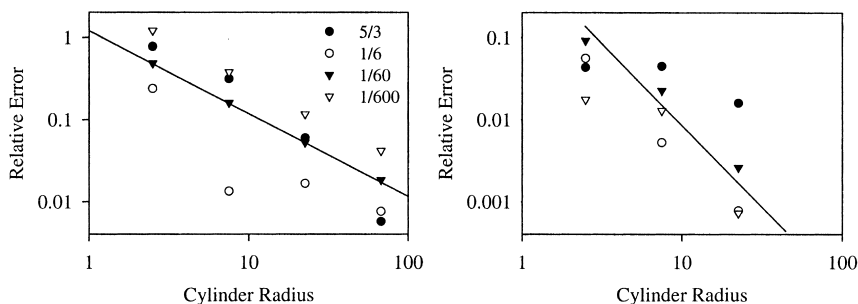


Fig. 7. Relative errors in the drag coefficient of a periodic array of cylinders at zero Reynolds number. The errors are computed for different cylinder radii and for different fluid viscosities, using the numerical solutions of Ref.⁽¹⁰⁷⁾ as a reference. The different symbols correspond to the values of the kinematic viscosity indicated in the legend. The convergence obtained using the nominal radius of the cylinder (left figure) can be compared with that obtained using the hydrodynamic radius of the cylinder (right figure). The straight lines in the left and right figures have slopes of -1 and -2 respectively.

the smallest viscosity, the relative error in the drag force is more than 5%, even for the largest particle ($a = 67.5$). It is clear that the shift in the location of the hydrodynamic boundary must be accounted for if quantitative results are to be obtained with computationally useful particle sizes (typically less than 10 lattice units) and viscosities significantly different from $1/6$. The right hand figure shows that once the hydrodynamic radius is taken into account, the errors in the drag force are reduced by an order of magnitude. Moreover the convergence is now almost quadratic in the resolution, except for the largest fluid viscosity, $\nu = 5/3$ ($\tau = 5.5$). In this case the slip velocity is rather large, as it is for a flat surface.

6.3. Continuous Bounce-Back Rules

A substantial effort has been invested to improve upon the accuracy of the bounce-back boundary condition at planar walls, typically using information from neighboring nodes to predict the non-equilibrium distribution at the boundary nodes.^(24, 36, 87, 91, 98, 112) A variant of these schemes uses the full velocity distribution function at a node to deduce the local velocity gradient.⁽⁴⁶⁾ These methods share the drawback that they require information about the shape of the particle surface. For general three-dimensional objects, the resulting algorithms are complex and not necessarily well defined without additional constraints.^(87, 98) As a result these methods have only been applied to planar surfaces and two-dimensional objects. By contrast, the bounce-back rule can be applied to surfaces of arbitrary shape, without additional complications. However, for second-order convergence the bounce-back rule requires a calibration of the hydrodynamic radius, which is not always convenient.

The bounce-back method enforces the no-slip boundary condition by controlling the momentum flux at the solid-fluid interface. More sophisticated variants of this scheme can be constructed, which take better account of curved and misaligned surfaces,^(21, 121) but still control the momentum flux rather than the distribution function. Extrapolation based methods^(24, 36, 87, 91, 98, 112) are problematic if two surfaces are in close proximity, which is a common occurrence in multi-particle suspensions, whereas flux control methods are completely local. Recently we have developed a modification of the bounce-back rule to account for partially filled cells.⁽¹²¹⁾ The method uses a volumetric formulation,^(6, 19) where the population density is assumed to be distributed throughout the Wigner-Seitz cell surrounding the lattice-node. It retains an important feature of the bounce-back rule, in that it does not require surface normals. Instead it represents the effects of an inclined plane by a sequence of partially filled cells, as

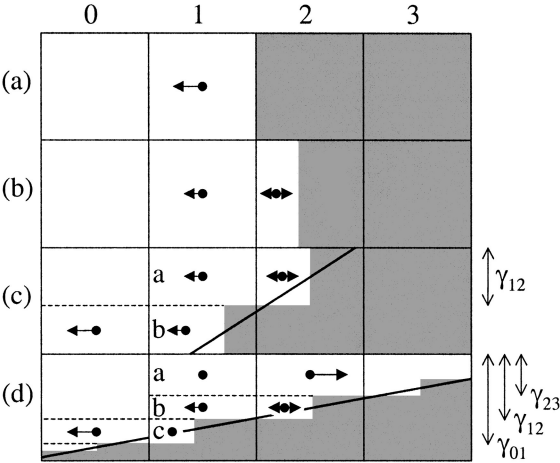


Fig. 8. Schematic representation of the different geometries discussed in the text. The gray areas represent the solid phase, and the arrows indicate the population densities after propagation of a population density in cell 1 moving from left to right. The solid dots indicate the location of the mean population density in each cell or fraction of a cell. The heavy lines in (c) and (d) indicate an inclined boundary represented by the sequence of partially filled cells. (Reprinted from ref. 121).

shown in Fig. 8. Although the method may be less accurate than that described in ref. 21, it has the advantages of simplicity and flexibility, and can be easily applied to irregular geometries.

The basic idea of the method, which we call “continuous bounce back”, can be understood from the sequence of diagrams in Fig. 8, showing the reflection of an incoming population density moving from left to right. In (a) the interface lies midway between the lattice nodes, as in the link bounce-back method; here the volumetric interpretation reduces to the link bounce-back method. Fig. 8(b) illustrates the volumetric rule in the simplest partial node case, with a population density propagating from cell 1 into a partially filled cell 2, with fluid fraction α_2 . Here a fraction $1 - 2\alpha_2$ is reflected back into cell 1, a fraction α_2 is reflected in cell 2, and a fraction α_2 propagates to cell 2, but is not reflected. The updated population densities are calculated assuming a linear variation in population density from cell 1 to cell 2, which is necessary for second-order accuracy in offset channels.

In Fig. 9a, we show the velocity profile for Poiseuille flow in a channel of width $L = 3\Delta x$, with the boundaries displaced from the lattice by a fraction of Δx . The agreement with the analytic result is surprisingly good,

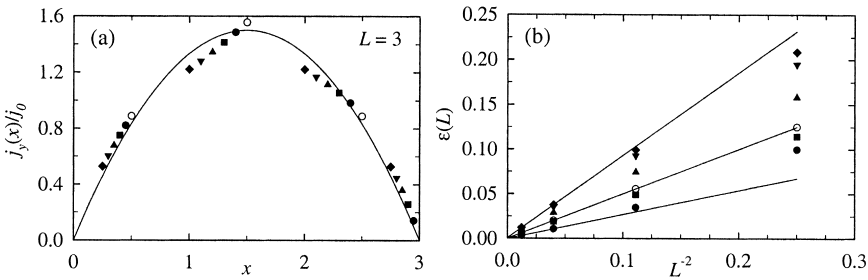


Fig. 9. Poiseuille flow in a shifted channel. a) Flow profile $j(x)$ for a channel-width $L = 3\Delta x$; the theoretical mean momentum flow $j_0 = L^2 \nabla p / 12\nu$. b) Mean relative error $\epsilon(L)$ in the flow profile. The open circles are the simulation results where the walls coincide with the interface between two cells. The solid symbols are for walls shifted with respect to the lattice in increments of $\Delta x/10$: in increasing order these go from solid circles ($0.1\Delta x$) to diamonds ($0.5\Delta x$). The solid lines indicate the asymptotic $1/L^2$ decay of $\epsilon(L)$. (Reprinted from ref. 121).

even though the channel is narrow; the largest deviations occur for channels shifted by $\frac{1}{2}\Delta x$ and are of the order of 10%. The mean relative error in the flow profile decreases as $1/L^2$, as shown in Fig. 9b. For $L \geq 5\Delta x$, $\epsilon(L)$ is less than 4%, while the error in the location of the hydrodynamic boundary is less than 0.05 lattice spacings. We obtained similar results for Poiseuille flow in channels of non-integer widths.

In most situations of practical interest the system changes rapidly from fluid to solid, typically with only one partially filled cell in between. However, more complicated geometries do arise, in which the solid-fluid interface extends over more than one cell. We approximate an inclined boundary extending over two cells by the geometry shown in Fig. 8c, so that during the propagation step a fraction of the population density is reflected in cell 1, while the remainder is reflected in cell 2. The height γ_{12} is determined by continuity between the two cells. The propagation rule now consists of the sum of two contributions, each of them determined by the same basic rules discussed in reference to Fig. 8b and multiplied by appropriate fractional weights. More general geometries (Fig. 8d) are handled by straightforward extensions of these rules; details of the method can be found in ref. 121. It should be noted that although the assignment of the heights $\gamma_{ij} = \frac{1}{2}(\alpha_i + \alpha_j)$ is non-local, extending over a maximum of 4 cells, the actual lattice-Boltzmann update is a sequence of local updates applied to pairs of population densities.

The continuous-bounce-back rules extend second-order convergence to channels of non-integer width, but in angled channels the convergence is still only first order. Nevertheless, the magnitude of the error is reduced by

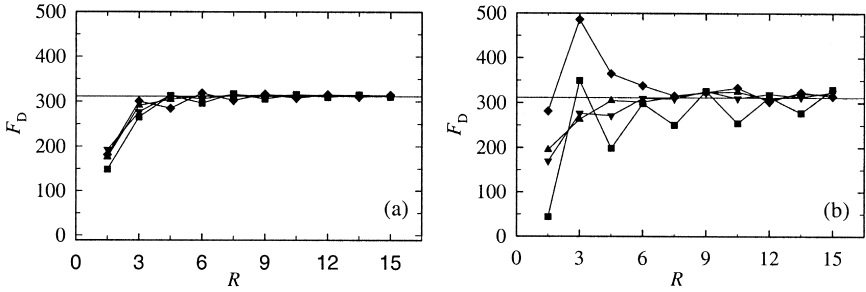


Fig. 10. Reduced drag coefficient F_D of a square array of disks, obtained with the continuous bounce-back rules (a) and link bounce-back rules (b), for different positions of the center of the disk with respect to the lattice: in the center of a cell (◆), in the corner of a cell (■) and at two random positions (▲ and ▼). The solid line is the theoretical result ⁽¹⁰⁷⁾ at the same porosity, $9\pi/64 = 0.442$. (Reprinted from ⁽¹²¹⁾).

up to a factor of 5 for a given channel width. The new rules have been tested by simulating fluid flow through periodic arrays of disks and spheres, which utilize a mixture of the different types of boundary configurations. In Fig. 10, the reduced drag coefficient of a square array of disks,

$$F_D = -L^2 \nabla p / \eta \langle u \rangle, \tag{67}$$

has been plotted as a function of the radius of the disk $R = 3L/8$. The results show two important improvements over the link bounce-back method: i) The drag coefficient obtained with the continuous bounce-back rules is virtually independent of the position of the center of the disk with respect to the lattice, and ii) the error in F_D is much smaller and the convergence to the asymptotic value is second order. For a cubic array of spheres the spread in F_D is even smaller than for disks, most probably due to a higher degree of averaging over the different types of boundaries. However, if the relaxation time is reduced to simulate higher Reynolds number flows, then the hydrodynamic radius will again differ from the physical one.

The new boundary rules allow for a reduction in resolution in typical simulations by a factor of two to four; in three dimensional simulations a factor of two reduction in resolution translates into at least a 16-fold reduction in computer time and an 8-fold reduction in memory. Although the continuous bounce-back rules are more complicated to implement than link bounce back rules, the additional computational overhead is small. We have combined the continuous bounce-back rules with a direct solution of the Stokes equations, ⁽¹²⁰⁾ to obtain a very fast algorithm for calculating fluid flow in porous media. The time taken to calculate the velocity field

in a realistic fracture geometry has been reduced from 400 hours to 3.5 hours.⁽¹²²⁾ Finally, we expect that the method can also be adopted to simulations of particle suspensions by modifying the reflected population densities to take account of the moving interface.⁽⁶⁹⁾

7. HYDRODYNAMIC INTERACTIONS

The generalization of the bounce-back rule to describe moving surfaces⁽⁷⁴⁾ made quantitative lattice-gas and lattice-Boltzmann simulations of particle suspensions possible. To understand the physics of the moving boundary condition, one can imagine an ensemble of particles, moving at constant speed c_i , impinging on a massive wall oriented perpendicular to the particle motion. The wall itself is moving with velocity $u_b \ll c_i$. The velocity of the particles after collision with the wall is $-c_i + 2u_b$ and the force exerted on the wall is proportional to $c_i - u_b$. Since the velocities in the lattice-Boltzmann model are discrete, the desired boundary condition cannot be implemented directly, but we can instead modify the density of returning particles so that the momentum transferred to the wall is the same as in the continuous velocity case. This is the essence of the physics, described somewhat differently, in refs. 69 and 74. The stochastic version of the rule was derived first,⁽⁷⁴⁾ allowing for the discrete population density that characterizes lattice-gas models.

7.1. Moving Boundary Condition

At each boundary node (see Fig. 6) there are two incoming distributions $n_i^*(\mathbf{r}, t)$ and $n_{i'}^*(\mathbf{r} + \mathbf{c}_i \Delta t, t)$, corresponding to velocities \mathbf{c}_i and $\mathbf{c}_{i'}$ ($\mathbf{c}_{i'} = -\mathbf{c}_i$) parallel to the link connecting \mathbf{r} and $\mathbf{r} + \mathbf{c}_i \Delta t$; the notation $n_i^*(\mathbf{r}, t) = n_i(\mathbf{r}, t) + \Delta_i(\mathbf{r}, t)$ is again used to indicate the post-collision distribution (Eq. 25). In some cases boundary nodes for two perpendicular links may be coincident (see Fig. 6); these are treated independently. The velocity of each boundary node, \mathbf{u}_b , is determined by the solid particle velocity \mathbf{U} , angular velocity $\mathbf{\Omega}$, and center of mass \mathbf{R} ,

$$\mathbf{u}_b = \mathbf{U} + \mathbf{\Omega} \times (\mathbf{r}_b - \mathbf{R}), \quad (68)$$

where $\mathbf{r}_b = \mathbf{r} + \frac{1}{2} \mathbf{c}_i \Delta t$. By exchanging population density between n_i and $n_{i'}$, we can modify the local momentum density of the fluid to match the velocity of the solid particle surface at the boundary node, without affecting either the mass density or the stress, which depend only on the sum $n_i + n_{i'}$.

The mechanism for boundary-node interactions is illustrated in Fig. 11. In Fig. 11a the incoming populations at a stationary node are reflected

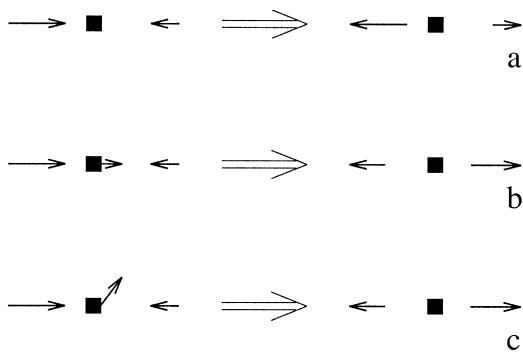


Fig. 11. Population densities before and after collision with a boundary node. The effects of stationary (a) and moving (b and c) boundary nodes on the incoming populations are shown. The arrows indicate the velocity direction and the lengths of the solid lines are proportional to the population densities. The differences between population densities are highly exaggerated for clarity. Note that the effects of the moving boundary are the same in (b) and (c), because the velocity component parallel to the link direction is the same in both cases. (Reprinted from ref. 69).

back in the direction they came from, which is just the link-bounce-back rule. For a moving node (Figs. 11b and 11c), population density is transferred across the boundary node, in proportion to the velocity of the node \mathbf{u}_b ,

$$\begin{aligned} n_i(\mathbf{r} + \mathbf{c}_i \Delta t, t + \Delta t) &= n_i^*(\mathbf{r} + \mathbf{c}_i \Delta t, t) + \frac{2a^{c_i} \rho \mathbf{u}_b \cdot \mathbf{c}_i}{c_s^2}, \\ n_i'(\mathbf{r}, t + \Delta t) &= n_i^*(\mathbf{r}, t) - \frac{2a^{c_i} \rho \mathbf{u}_b \cdot \mathbf{c}_i}{c_s^2}. \end{aligned} \tag{69}$$

Only the velocity component along the link direction ($\mathbf{u}_b \cdot \mathbf{c}_i$) is included in the calculation of population transfer; thus the outcomes in Figs. 11b and 11c are the same, while for stationary nodes ($\mathbf{u}_b = 0$) the bounce-back condition is recovered. The coefficient of the $\mathbf{u}_b \cdot \mathbf{c}_i$ term is determined by the requirement that any distribution consistent with the boundary-node velocity \mathbf{u}_b is stationary with respect to interactions with the boundary nodes. For example, the distribution $n_i(\mathbf{r}, t + \Delta t)$ can be written in terms of the moments of the distribution $\mathbf{n}(\mathbf{r}, t)$, using Eqs. 25 and 69:

$$\begin{aligned} n_i(\mathbf{r}, t + \Delta t) &= n_i(\mathbf{r}, t) \\ &+ \frac{a^{c_i}}{2c_s^4} \left(\lambda \bar{\Pi}^{neq} + \frac{\lambda_v}{3} (\Pi^{neq} : \mathbf{1}) \mathbf{1} \right) : (\mathbf{c}_i \mathbf{c}_i - c_s^2 \mathbf{1}) - \frac{2a^{c_i} \rho \mathbf{u}_b \cdot \mathbf{c}_i}{c_s^2}. \end{aligned} \tag{70}$$

For times longer than t_1 , the non-equilibrium momentum flux Π^{neq} can be replaced by a velocity gradient (Eq. 40),

$$\begin{aligned} n_i(\mathbf{r}, t + \Delta t) - n_i(\mathbf{r}, t) \\ = \frac{a^c \rho}{c_s^2} (\mathbf{c}_i \cdot \nabla \mathbf{u} \cdot \mathbf{c}_i \Delta t - c_s^2 \nabla \cdot \mathbf{u} \Delta t - 2\mathbf{u}_b \cdot \mathbf{c}_i). \end{aligned} \quad (71)$$

In addition, Eq. 25 can be used to replace $n_i(\mathbf{r}, t)$ with $n_i(\mathbf{r}, t) + 2a^c \rho \mathbf{u} \cdot \mathbf{c}_i / c_s^2$, and since $\mathbf{u}_b = \mathbf{u} + \frac{1}{2} \mathbf{c}_i \cdot \nabla \mathbf{u} \Delta t + \dots$,

$$n_i(\mathbf{r}, t + \Delta t) - n_i(\mathbf{r}, t) = -a^c \rho \nabla \cdot \mathbf{u} \Delta t = a^c \partial_i \rho \Delta t + \mathcal{O}(M^2). \quad (72)$$

Thus for stationary flows Eq. 69 is consistent with a boundary-node velocity, \mathbf{u}_b . It should be noted that the local density $\rho(\mathbf{r}, t)$ appears in the equation for the moving boundary condition (Eq. 69), but we have typically used the mean density (ρ_0) instead, since it simplifies the update procedure. The differences between the two methods are small, of the same order (ρu^3) as the error terms in Eq. 38. Test calculations show that even large variations in fluid density (up to 10%) have a negligible effect on the force (less than 1 part in 10^4).

As a result of the boundary node updates, momentum is exchanged locally between the fluid and the solid particle, but the combined momentum of solid and fluid is conserved. The forces exerted at the boundary nodes can be calculated from the momentum transfer in Eq. 69,

$$\mathbf{f}\left(\mathbf{r}_b, t + \frac{1}{2} \Delta t\right) = \frac{2\Delta x^3}{\Delta t} \left[n_i^*(\mathbf{r}, t) - n_i^*(\mathbf{r} + \mathbf{c}_i \Delta t, t) - \frac{2a^c \rho \mathbf{u}_b \cdot \mathbf{c}_i}{c_s^2} \right] \mathbf{c}_i. \quad (73)$$

The particle forces and torques are obtained by summing $\mathbf{f}(\mathbf{r}_b)$ and $\mathbf{r}_b \times \mathbf{f}(\mathbf{r}_b)$ over all the boundary nodes associated with a particular particle. It can be shown analytically that the force on a moving wall in a linear shear flow is exact,⁽⁶⁹⁾ and several numerical examples of lattice-Boltzmann simulations of hydrodynamic interactions are given in ref. 70.

The velocity-dependent bounce-back rule can also be implemented using nodal bounce-back boundary conditions.^(74, 75) However in this case, the moving bounce-back rule must also be applied to nodes inside the particle surface. This can lead to a pressure drop in the gap between two closely-spaced particles and thereby cause an artificial attraction between the particles.⁽⁵⁾

7.2. Lubrication

When two spheres approach each other there is a strong repulsive force, caused by fluid being squeezed out of the gap between the particles. These lubrication flows generate very high pressures in the gap, which are difficult to resolve with either a grid-based code or a multipole code. Although it is possible to use adaptive meshes to resolve the flow in the gap, a more computationally tractable solution is to calculate the singular forces separately by lubrication theory.⁽³¹⁾ This idea has been incorporated into a lattice-Boltzmann model,⁽⁷²⁾ adding the normal lubrication force between two spheres:

$$\mathbf{F}_{ij}^{lub} = -\frac{6\pi\eta(aa')^2}{(a+a')^2} \hat{\mathbf{R}}_{ij} \hat{\mathbf{R}}_{ij} \cdot (\mathbf{u}_i - \mathbf{u}_j) \left(\frac{1}{R_{ij} - a - a'} - \frac{1}{\Delta_c} \right), \quad (74)$$

where a and a' are the radii of the spheres.³ Δ_c is the cut off for the added lubrication force; for gaps $(R_{ij} - a - a')$ larger than Δ_c the lattice-Boltzmann model captures the full hydrodynamic interactions between the spheres, and $\mathbf{F}_{ij}^{lub} = 0$. Recent research has shown that a value of $\Delta_c = \frac{2}{3} \Delta x$ is suitable for all sphere sizes.⁽⁹⁶⁾ This is quite consistent with earlier work,⁽⁷⁰⁾ which showed that the lattice-Boltzmann method reproduced the hydrodynamic interactions between pairs of spheres down to gaps of 1 lattice spacing. Figure 12 shows lattice-Boltzmann simulations of the lubrication interaction between a sphere and a plane wall. The lattice-Boltzmann simulations (solid symbols) agree almost perfectly with the exact solution⁽¹⁴⁾ down to gaps less than 1 lattice spacing. Thus for successively larger particles, the lubrication force can be calculated at smaller and smaller gaps, relative to the particle size. Including the short-range lubrication force (Eq. 74 with $a' = \infty$ and $\Delta_c = \frac{2}{3} \Delta x$) brings about almost perfect agreement with Brenner's solution⁽¹⁴⁾ for spheres more than about 5 lattice spacings in diameter (open symbols). The tangential lubrication can be included in a similar fashion, using the appropriate expressions for the singular forces and torques.^(28, 61) Tangential forces have a weaker logarithmic divergence, and here the optimum cut off was found to be $\Delta_c = \Delta x$,⁽⁹⁶⁾ again independent of particle size.

The lubrication forces can be large for particles pushed close to contact, and an explicit velocity update⁽⁶⁹⁾ is quite unstable. We have therefore developed an implicit pair-by-pair update of the lubrication interactions,⁽⁹⁶⁾ which is stable for all particle separations. Assuming that the particle coordinates are essentially unchanged during a single time step,

³ Equation 9 of ref. 72 is missing a factor of 2 in the denominator.

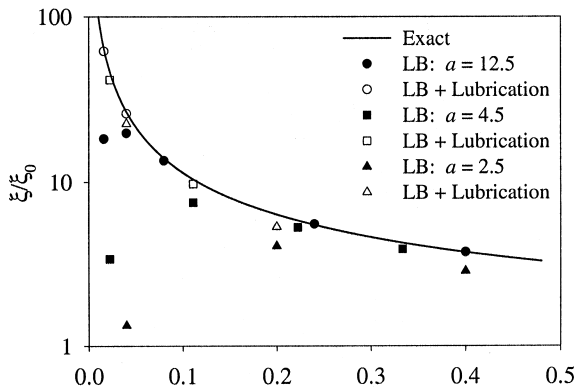


Fig. 12. Lubrication forces normal to a plane wall. The friction coefficients (ξ) from lattice-Boltzmann simulations are compared with exact solutions of the Stokes equations; $\xi_0 = 6\pi\eta a$ is the Stokes drag coefficient.

the relative velocity of a pair of spheres can be found from the ordinary differential equation

$$m\dot{u}_{ij} = -\zeta u_{ij}, \tag{75}$$

where ζ is a configuration-dependent friction coefficient, taken from Eq. 74, and u_{ij} is the relative velocity projected along the line of centers. The relative velocity at the end of the time step is then simply related to that at the beginning of the step, $u_{ij}(\Delta t) = u_{ij}(0) e^{-\zeta\Delta t/m}$. By transforming to a coordinate system where the separation vector \mathbf{R}_{ij} is parallel to one of the principal axes,⁽²⁸⁾ the complete lubrication interaction between a pair of spheres can be updated implicitly by solving coupled pairs of ordinary differential equations.

When two particles are close to contact, it can happen that they share a common boundary node. As they move towards each other, these particles should be expelling fluid from their interior, giving rise to a high pressure in the gap between the two surfaces, but the absence of a fluid node between the surfaces prevents this from happening. The missing forces can be compensated for as described above, but these shared nodes also upset the overall mass balance between fluid flowing into and out of the particle. When shared nodes occur, there can be a slow loss or gain of fluid from the interior of the particle, preventing the system coming to steady state. We have found that the best solution is to first determine the total mass transfer across the particle surface, which in the absence of shared nodes is identically zero. Any excess mass can be uniformly distributed over the boundary nodes, with only a very small change in the force

and torque. The drawback of this procedure is that it requires an extra pass over the boundary nodes, but it allows the particles to smoothly approach one another, all the way to contact.

7.3. Inertia

The lattice-Boltzmann method works without modification for flows where the Reynolds number is non-zero, although as the Reynolds number increases, larger particles are required for the same accuracy.⁽⁶³⁾ Here we show one example of a finite Reynolds number flow, examining the lift force on a cylinder in close proximity to a plane wall.⁽⁶⁰⁾ Lattice-Boltzmann simulations of the drag and lift forces on the cylinder are shown in Fig. 13 and compared with accurate finite-difference calculations⁽⁶⁰⁾ under the same flow conditions. The simulations were carried out for two different cylinder sizes, and drag coefficients were calculated down to a gap of 1 lattice spacing between the particle and the wall. It can be seen from Fig. 13 that the drag coefficients are in essentially exact agreement with the finite-difference calculations. However, the lift force is a much more sensitive test of the simulation, since it is a purely inertial effect and vanishes in the low Reynolds number limit. It is encouraging that quantitative agreement is obtained in this case as well; the only significant deviation is for the smaller cylinder at a distance of 1 lattice spacing from the wall. Quantitative comparisons of dynamic simulations with corresponding finite-element calculations have also been reported.^(2, 103)

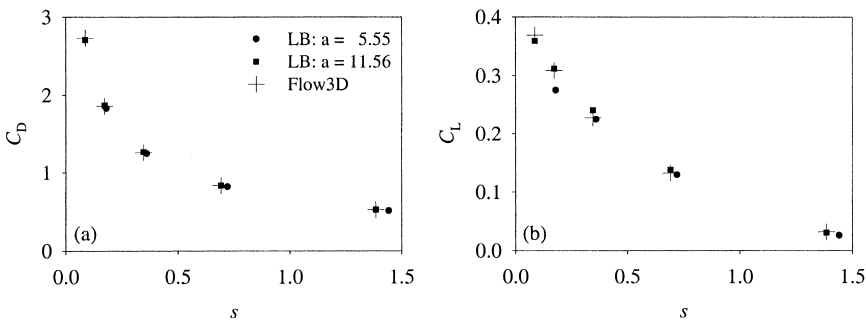


Fig. 13. Lift force on a cylinder (radius a) near a moving planar boundary (velocity U) at a Reynolds number $Re = 7$. The dimensionless coefficients $C = F/(\pi a \rho U^2)$ (F is the force per unit length on the cylinder) are shown for the drag force (left) and lift force (right). The results of lattice-Boltzmann simulations⁽⁶⁰⁾ are compared with finite-element calculations in an identical geometry.

7.4. Interior Fluid

In accounting for the momentum transfer at a moving wall, mass is locally conserved by the presence of the interior fluid. The particles comprise a solid shell of given mass and inertia, filled with fluid of the same mass density as the bulk fluid. It has been claimed that this model is unphysical,⁽¹⁾ but the pertinent issue is to what extent do the dynamics of these fluid-filled particles differ from the dynamics of solid particles. This question was addressed in section 5 of ref. 70; here we summarize the important findings. The parameter characterizing the motion of the interior fluid is the non-dimensional frequency $\omega^* = \omega a^2 / \nu_{int}$ where a is the sphere radius and ν_{int} is the kinematic viscosity of the interior fluid, which can be different from that in the exterior flow region. Numerical results show that the drag force on an oscillating sphere is independent of the interior fluid as long as $\omega^* < 1$. The reduced frequency can be made arbitrarily small by increasing the viscosity of the interior fluid. Furthermore, it was shown that to lowest order in the frequency, flow in the interior fluid contributes a viscosity independent term that is exactly equal to the inertia of the interior fluid. Deviations from the inertial drag are generally small, proportional to the square of the frequency to leading order. Thus the particle behaves dynamically as if its mass is the sum of the shell mass, used to compute the change in shell velocity arising from hydrodynamic forces, and the mass of the interior fluid. Effects of the interior fluid on the particle dynamics are small so long as the contribution of the interior fluid to the inertia of the particle is taken into account.

Alternative methods have been proposed in which fluid is excluded from the interior of the particle,^(2, 55) which then behaves as a solid object described by its shell mass and inertia. The change in local mass density is proportional to the local velocity of the boundary node and averages to zero when summed over the whole particle surface. However global mass conservation may be violated when two surfaces are close to contact, without intervening fluid (*c.f.* Section 7.2). Attempts to maintain local mass conservation without interior fluid⁽¹⁾ are fundamentally flawed, and lead to incorrect pressure distributions around the solid particle. More recent simulations⁽²⁾ show excellent agreement between lattice-Boltzmann simulations and finite-element calculations,⁽³⁴⁾ independent of the presence or absence of interior fluid, so long as the shell mass and inertia are adjusted accordingly. Thus we conclude that accurate simulations can be carried out with or without interior fluid.

There are drawbacks to both of these schemes. The instantaneous fluctuations of fluid-filled particles are larger than those of solid particles with the same total mass, since the interior fluid does not have sufficient

time to respond to changes in velocity of the shell. On the other hand, if the interior fluid is excluded, it is then necessary to add fluid with the correct mass and momentum density to solid sites being vacated as the particle moves, and to similarly remove fluid from sites being covered by the particle. A perturbation is thereby added to the fluid flow whenever a particle changes position. Nevertheless, it should be emphasized that both methods give results in good agreement with one another and with independent finite-element simulations.⁽²⁾ An alternative method of removing the effects of the interior fluid has been proposed recently.⁽⁵⁵⁾ Here the boundary nodes are updated as in Eq. 69, but the momentum thus transferred to the interior fluid is later put back into the particle and the interior fluid momentum is reset to zero. While this method works very well for particles that do not move with respect to the grid,⁽⁵⁵⁾ it remains to be seen if this method or that proposed in ref. 2 move the particles across the mesh as smoothly as the method described in ref. 72.

7.5. Velocity Update

In ref. 70 particle velocities were determined from an explicit update,

$$U(t + \Delta t) = U(t - \Delta t) + \frac{2F(t) \Delta t}{M}, \tag{76}$$

where velocities are updated every other time step to minimize the effects of the staggered momentum invariants.⁽⁹⁰⁾ There is a stability criterion for Eq. 76 and its rotational equivalent,⁽⁷⁰⁾ which can be expressed as a condition on the effective mass density of the solid particle (including the mass of the interior fluid),

$$\frac{\rho_s}{\rho_f} > 1 + \frac{10}{a}. \tag{77}$$

This stability criterion imposes a serious constraint on the size of particles which can be used to simulate realistic particle-fluid systems for which $\rho_s/\rho_f \approx 2$. However, an implicit velocity update has been proposed⁽⁸³⁾ that is unconditionally stable. Schematically,

$$U(t + \Delta t) - U(t) = \frac{[F_0(t) - \lambda U(t + \Delta t)] \Delta t}{M}, \tag{78}$$

where $F_0(t)$ is the part of the particle force arising from the zero-velocity bounce-back rule and $\lambda U(t + \Delta t)$ comes from the velocity-dependent part of

the boundary update.⁽⁷⁰⁾ The coefficient λ resembles a friction coefficient, and is determined by the distribution of boundary nodes on the particle surface. An explicit update replaces the unknown velocity $U(t + \Delta t)$ on the right-hand side of Eq. 78 by $U(t)$ (as in Eq. 76), but an unconditionally stable update can be achieved by solving Eq. 78 for $U(t + \Delta t)$ directly. The drawback of this new scheme is that it takes two sweeps through the boundary nodes. The first sweep is used to determine F_0 so that $U(t + \Delta t)$ can be found; this involves solving six coupled equations for the translational and rotational velocities of each particle. The second sweep uses the new velocities to finish the boundary node updates.

Further complications arise when we consider the consequences of particle displacements. One possibility is to keep track of the actual particle coordinates but only update the boundary node positions when the particle center moves nearer to an adjacent lattice site than to its current one. Thus the boundary-node map is always centered on a lattice node and the particle shape is constant in time (for spherical particles). This approach has two drawbacks. The first problem is that the translation of the boundary node map by a distance of the order of one lattice spacing introduces a significant discontinuity into the fluid flow. The second problem is that an additional check is required before the boundary node map is moved, to ensure that there are no overlapping maps. Even in moderately dense suspensions this leads to “traffic jams” with boundary node maps that are unable to move to the correct locations. A better solution is to move the boundary-node maps continuously, so that discontinuities in fluid motion are small and traffic jams do not arise. In this case the particle shape fluctuates with changes in particle position, but the effects of these shape fluctuations are small if the particle radius is more than about $5\Delta x$. Fluctuations in particle shape can be minimized by using continuous bounce-back collision rules⁽¹²¹⁾ (see Section 6.3).

8. FLUCTUATIONS

The lattice-Boltzmann model can be extended to simulate thermal fluctuations, which lead to Brownian motion of colloidal particles. The fluctuating lattice-Boltzmann model⁽⁶⁸⁾ incorporates a random component into the momentum flux during the collision process (*c.f.* Eq. 26):

$$\begin{aligned}\Pi^{neq, \star} &= (1 + \lambda) \bar{\Pi}^{neq} + \frac{1}{3} (1 + \lambda_v) (\Pi^{neq} : \mathbf{1}) \mathbf{1} + \Pi^f \\ \Pi^f &= \zeta \bar{\mathbf{R}} + \zeta_v \mathbf{R}_v \mathbf{1},\end{aligned}\tag{79}$$

where R_v is a Gaussian random variable with zero mean and unit variance, and \mathbf{R} is a symmetric matrix of Gaussian random variables of zero mean. The off-diagonal elements of \mathbf{R} have a variance of 1, while the diagonal elements have a variance of 2. In this particular implementation, 6 random numbers are required to generate the components of the symmetric matrix \mathbf{R} , together with the constraint that $\bar{\mathbf{R}}$ is traceless. The average stress fluctuations are local in space and time, as in Eq. 4, with a variance given by

$$\langle \Pi_{\alpha\beta}^f \Pi_{\gamma\delta}^f \rangle = \zeta^2 (\overline{\delta_{\alpha\gamma} \delta_{\beta\delta}} + \overline{\delta_{\alpha\delta} \delta_{\beta\gamma}}) + \zeta_v^2 \delta_{\alpha\beta} \delta_{\gamma\delta}. \tag{80}$$

An analogy with Eq. 4 suggests that

$$\zeta = \left(\frac{2k_B T \eta}{\Delta x^3 \Delta t} \right)^{1/2} \quad \zeta_v = \left(\frac{2k_B T \eta_v}{\Delta x^3 \Delta t} \right)^{1/2}, \tag{81}$$

but it will be seen that the discrete lattice again modifies the result for continuous fluids,⁽⁶⁹⁾ so that Eq. 81 is not entirely correct. Instead, the coefficients will be determined by relating the decay of long wavelength stress fluctuations to the viscosity of the lattice-Boltzmann fluid.

8.1. Discrete Green–Kubo Relation

The volume integral of the stress,

$$\Sigma(t) = -\Delta x^3 \sum_{\mathbf{r} \in V} [\Pi(\mathbf{r}, t) - \Pi^{eq}(\mathbf{r}, t)], \tag{82}$$

is only affected by collisions and not by propagation of particle densities. The time evolution of Σ can therefore be written as

$$\Sigma(t + \Delta t) = (1 + \lambda) \bar{\Sigma}(t) + \frac{1}{3} (1 + \lambda_v) (\Sigma(t) : \mathbf{1}) \mathbf{1} + \Sigma^f(t), \tag{83}$$

where $\Sigma^f(t) = -\Delta x^3 \sum_{\mathbf{r} \in V} \Pi^f(\mathbf{r}, t)$ is the random stress. Equation 83 is a discrete Langevin equation of the form

$$s(t + \Delta t) - s(t) = -\alpha s(t) + f(t), \tag{84}$$

with random force $f(t)$ and $\alpha > 0$. It is shown in the Appendix of ref. 69 that

$$\langle s(n\Delta t) s(0) \rangle = (1 - \alpha)^n \langle s^2 \rangle, \tag{85}$$

and that fluctuations in s are related to fluctuations in f by

$$\langle s^2 \rangle = \frac{\langle f^2 \rangle}{2\alpha - \alpha^2}. \quad (86)$$

Combining Eqs. 85 and 86 we obtain the discrete equivalent of the time-integral of the correlation function $\int_0^\infty \langle s(t) s(0) \rangle dt$, namely

$$\frac{1}{2} \langle s^2 \rangle + \sum_{t=\Delta t}^\infty \langle s(t) s(0) \rangle = \left(\frac{1}{\alpha} - \frac{1}{2} \right) \langle s^2 \rangle = \frac{\langle f^2 \rangle}{2\alpha^2}. \quad (87)$$

Similarly, the low-frequency correlations of the integrated stress $\Sigma(t)$ are related to the instantaneous fluctuations in the random stress $\langle \Sigma^f \Sigma^f \rangle = N \Delta x^6 \langle \Pi^f \Pi^f \rangle$,

$$\begin{aligned} \frac{1}{2} \langle \Sigma_{\alpha\beta} \Sigma_{\gamma\delta} \rangle + \sum_{t=\Delta t}^\infty \langle \Sigma_{\alpha\beta}(t) \Sigma_{\gamma\delta}(0) \rangle \\ = \frac{\zeta^2 V \Delta x^3}{2\lambda^2} (\overline{\delta_{\alpha\gamma} \delta_{\beta\delta}} + \overline{\delta_{\alpha\delta} \delta_{\beta\gamma}}) + \frac{\zeta_v^2 V \Delta x^3}{2\lambda_v^2} \delta_{\alpha\beta} \delta_{\gamma\delta}, \end{aligned} \quad (88)$$

where the number of lattice points in the fluid $N = V / \Delta x^3$.

The left hand side of Eq. 88 is the discrete equivalent of the Green-Kubo integral⁽⁵⁰⁾ relating the viscosity to equilibrium fluctuations in the stress; for example

$$\eta = \frac{1}{V k_B T} \int_0^\infty \langle \Sigma_{xy}(t) \Sigma_{xy}(0) \rangle dt. \quad (89)$$

The stress fluctuations in the fluctuating lattice-Boltzmann model can be made consistent with the discrete Green-Kubo formula,

$$\begin{aligned} \frac{1}{2} \langle \Sigma_{\alpha\beta} \Sigma_{\gamma\delta} \rangle + \sum_{t=\Delta t}^\infty \langle \Sigma_{\alpha\beta}(t) \Sigma_{\gamma\delta}(0) \rangle \\ = \frac{\eta V k_B T}{\Delta t} (\overline{\delta_{\alpha\gamma} \delta_{\beta\delta}} + \overline{\delta_{\alpha\delta} \delta_{\beta\gamma}}) + \frac{\eta_v V k_B T}{\Delta t} \delta_{\alpha\beta} \delta_{\gamma\delta}, \end{aligned} \quad (90)$$

by an appropriate choice for the amplitudes of the random fluctuations in Eq. 88; *i.e.*

$$\zeta = \left(\frac{2k_B T \eta \lambda^2}{\Delta x^3 \Delta t} \right)^{1/2}, \quad \zeta_v = \left(\frac{2k_B T \eta_v \lambda_v^2}{\Delta x^3 \Delta t} \right)^{1/2}. \quad (91)$$

The additional factor of $\sqrt{\lambda^2}$ (*c.f.* Eq. 81) is a consequence of discrete lattice artifacts. For the choice of eigenvalues $\lambda = \lambda_v = -1$, an exact correspondence with the fluctuation-dissipation relation for continuous systems is obtained. However the discrete version (Eq. 91) can also be applied to systems where the viscous eigenvalues are not equal to -1 .⁽⁶⁹⁾

8.2. Momentum Fluctuations

In the previous Section (8.1) the discrete Green–Kubo formulae for the shear and bulk viscosity (Eq. 90) were obtained by replacing the time integral in Eq. 89 by a summation. Here it is shown that Eq. 90 can be derived directly from the instantaneous fluctuations in momentum density.⁽⁴¹⁾ Moreover, the connection between temperature and the strength of the random forcing is made clear. It will be more convenient to work in Fourier space, defining the Fourier transform of the velocity distribution function as

$$n'_i(\mathbf{k}, t) = \Delta x^3 \sum_{\mathbf{r} \in V} e^{-i\mathbf{k} \cdot \mathbf{r}} [n_i(\mathbf{r}, t) - \langle n_i \rangle], \quad (92)$$

where $\langle n_i \rangle = a^{c_i} \rho_0$ is the ensemble-averaged value of n_i . Again the volume of the cell associated with each node of the lattice-Boltzmann model has been included, to maintain consistency with the continuous Fourier integral.

The mass and momentum conservation equations (Eq. 32 without external forces) are Fourier transformed

$$\sum_i e^{i\mathbf{k} \cdot \mathbf{c}_i \Delta t} n'_i(\mathbf{k}, t + \Delta t) = \sum_i n'_i(\mathbf{k}, t) \quad (93)$$

$$\sum_i e^{i\mathbf{k} \cdot \mathbf{c}_i \Delta t} n'_i(\mathbf{k}, t + \Delta t) \mathbf{c}_i = \sum_i n'_i(\mathbf{k}, t) \mathbf{c}_i, \quad (94)$$

and expanded to order k^2 :

$$\begin{aligned} \delta \rho(\mathbf{k}, t + \Delta t) \\ + i\mathbf{k} \cdot \mathbf{j}(\mathbf{k}, t + \Delta t) \Delta t - \frac{1}{2} \mathbf{k} \mathbf{k} : \Pi(\mathbf{k}, t + \Delta t) \Delta t^2 = \delta \rho(\mathbf{k}, t), \end{aligned} \quad (95)$$

$$\begin{aligned} \mathbf{j}(\mathbf{k}, t + \Delta t) \\ + i\mathbf{k} \cdot \Pi(\mathbf{k}, t + \Delta t) \Delta t - \frac{1}{2} \mathbf{k} \mathbf{k} : \Psi(\mathbf{k}, t + \Delta t) \Delta t^2 = \mathbf{j}(\mathbf{k}, t), \end{aligned} \quad (96)$$

where $\Psi = \sum_i n'_i \mathbf{c}_i \mathbf{c}_i \mathbf{c}_i$ is the third moment of the distribution and $\delta\rho(\mathbf{k}, t) = \rho(\mathbf{k}, t) - \rho_0 V \delta_{\mathbf{k}, 0}$.

The momentum flux is decomposed into an equilibrium part, a viscous part, and a fluctuating part:

$$\Pi(\mathbf{k}, t) = \Pi^{eq}(\mathbf{k}, t) - \boldsymbol{\sigma}^c(\mathbf{k}, t) - \boldsymbol{\sigma}^f(\mathbf{k}, t), \quad (97)$$

where $\boldsymbol{\sigma}^c(\mathbf{k}, t)$ is the Fourier transform of the collisional stress tensor (Eq. 42)

$$\boldsymbol{\sigma}^c(\mathbf{k}, t) = v^c [\overline{i\mathbf{k}\mathbf{j}(\mathbf{k}, t)} + \overline{i\mathbf{j}(\mathbf{k}, t)\mathbf{k}}] + v_l^c i\mathbf{k} \cdot \mathbf{j}(\mathbf{k}, t) \mathbf{1}. \quad (98)$$

Equation 97 is a typical Langevin decomposition into slow ($\boldsymbol{\sigma}^c$) and fast ($\boldsymbol{\sigma}^f$) components. Thus $\boldsymbol{\sigma}^f$ is not equivalent to the random fluctuations in Eq. 79, but instead expresses the instantaneous deviations of the stress tensor from $\boldsymbol{\sigma}^c$. These deviations include the effects of random fluctuations at earlier times, which persist for times up to t_1 .

For small fluctuations from equilibrium, non-linear terms can be ignored and $\Pi^{eq}(\mathbf{k}, t) = \delta\rho(\mathbf{k}, t) c_s^2 \mathbf{1}$. Similarly, the effects of density fluctuations on the transport coefficients (*c.f.* Eq. 58) can also be neglected and the momentum flux written as

$$\begin{aligned} i\mathbf{k} \cdot \Pi(\mathbf{k}, t) \Delta t &= v^c k^2 \Delta t \mathbf{j}(\mathbf{k}, t) + (v_l^c - v^c) k^2 \Delta t \hat{\mathbf{k}} \hat{\mathbf{k}} \cdot \mathbf{j}(\mathbf{k}, t) \\ &\quad - i\mathbf{k} \cdot \boldsymbol{\sigma}^f(\mathbf{k}, t) \Delta t + i\mathbf{k} \delta\rho(\mathbf{k}, t) c_s^2 \Delta t. \end{aligned} \quad (99)$$

The kinematic viscosity coefficients v^c and $v_l^c = v_v^c + \frac{4}{3} v^c$ contain collisional contributions only (Eq. 43).

Since the kinetic modes relax rapidly (on a time scale Δt), the non-equilibrium contributions to the third moment are negligible and $\Psi_{\alpha\beta\gamma} = \Psi_{\alpha\beta\gamma}^{eq} = c_s^2 (\mathbf{j}_\alpha \delta_{\beta\gamma} + \mathbf{j}_\beta \delta_{\gamma\alpha} + \mathbf{j}_\gamma \delta_{\alpha\beta})$. This term contains the lattice contributions to the viscosity (Eq. 46), together with an additional term proportional to $\mathbf{k}\mathbf{k} \cdot \mathbf{j}$. Combining this result with Eq. 99,

$$\begin{aligned} i\mathbf{k} \cdot \Pi(\mathbf{k}, t) \Delta t - \frac{1}{2} \mathbf{k}\mathbf{k} : \Psi(\mathbf{k}, t) \Delta t^2 \\ &= v k^2 \Delta t \mathbf{j}(\mathbf{k}, t) + (v_l - v) k^2 \Delta t \hat{\mathbf{k}} \hat{\mathbf{k}} \cdot \mathbf{j}(\mathbf{k}, t) - i\mathbf{k} \cdot \boldsymbol{\sigma}^f(\mathbf{k}, t) \\ &\quad + i\mathbf{k} \delta\rho(\mathbf{k}, t) c_s^2 \Delta t - \frac{1}{2} \rho c_s^2 \Delta t^2 k^2 \hat{\mathbf{k}} \hat{\mathbf{k}} \cdot \mathbf{j}(\mathbf{k}, t). \end{aligned} \quad (100)$$

The mass conservation equation (Eq. 95) can be used to replace the last two terms on the right hand side by density fluctuations,

$$i\mathbf{k} \delta\rho(\mathbf{k}, t) - \frac{1}{2} \Delta t k^2 \hat{\mathbf{k}} \hat{\mathbf{k}} \cdot \mathbf{j}(\mathbf{k}, t) = \frac{1}{2} [i\mathbf{k} \delta\rho(\mathbf{k}, t) + i\mathbf{k} \delta\rho(\mathbf{k}, t - \Delta t)]. \quad (101)$$

Terms proportional to $\delta\rho$ vanish at small k and can be omitted from the momentum fluctuations. Although fluctuations in density and longitu-

dinal momentum are correlated at finite wavelengths, they are decoupled in the long-wavelength limit. The longitudinal $j_{\parallel} = \hat{\mathbf{k}} \cdot \mathbf{j}$ and transverse $\mathbf{j}_{\perp} = (\mathbf{1} - \hat{\mathbf{k}}\hat{\mathbf{k}}) \cdot \mathbf{j}$ components can be calculated separately:

$$j_{\parallel}(\mathbf{k}, t + \Delta t) - j_{\parallel}(\mathbf{k}, t) + v_l k^2 \Delta t j_{\parallel}(\mathbf{k}, t + \Delta t) = i k \Delta t \sigma_{\parallel}^f(\mathbf{k}, t + \Delta t) \quad (102)$$

$$\mathbf{j}_{\perp}(\mathbf{k}, t + \Delta t) - \mathbf{j}_{\perp}(\mathbf{k}, t) + v k^2 \Delta t \mathbf{j}_{\perp}(\mathbf{k}, t + \Delta t) = i k \Delta t \boldsymbol{\sigma}_{\perp}^f(\mathbf{k}, t + \Delta t). \quad (103)$$

Equations 102 and 103 are discrete Langevin equations, similar to Eq. 84, with random forces $\sigma_{\parallel}^f = \hat{\mathbf{k}} \cdot \boldsymbol{\sigma}^f \cdot \hat{\mathbf{k}}$ and $\boldsymbol{\sigma}_{\perp}^f = \hat{\mathbf{k}} \cdot \boldsymbol{\sigma}^f \cdot (\mathbf{1} - \hat{\mathbf{k}}\hat{\mathbf{k}})$. Unlike the integrated stress correlations (Eq. 83), here the random forces have finite correlation times, and the solution involves a Green-Kubo integral (see the Appendix of ref. 69),

$$2v_l \langle j_{\parallel}(\mathbf{k}) j_{\parallel}(-\mathbf{k}) \rangle = \Delta t \sum_{t=-\infty}^{\infty} \langle \sigma_{\parallel}^f(\mathbf{k}, t) \sigma_{\parallel}^f(-\mathbf{k}, 0) \rangle, \quad (104)$$

$$2v \langle \mathbf{j}_{\perp}(\mathbf{k}) \cdot \mathbf{j}_{\perp}(-\mathbf{k}) \rangle = \Delta t \sum_{t=-\infty}^{\infty} \langle \boldsymbol{\sigma}_{\perp}^f(\mathbf{k}, t) \cdot \boldsymbol{\sigma}_{\perp}^f(-\mathbf{k}, 0) \rangle. \quad (105)$$

In the long-wavelength limit, the fluctuating stress, $\lim_{\mathbf{k} \rightarrow 0} \boldsymbol{\sigma}^f(\mathbf{k}, t)$, is equal to the volume integral of the stress, $\boldsymbol{\Sigma}(t)$, since momentum fluctuations vanish. The right hand sides of Eqs. 104 and 105 can then be evaluated in the long-wavelength limit, using Eq. 88 to calculate the sums of the stress fluctuations:

$$2v_l \lim_{\mathbf{k} \rightarrow 0} \langle j_{\parallel}(\mathbf{k}) j_{\parallel}(-\mathbf{k}) \rangle = V \Delta x^3 \Delta t \left(\frac{4}{3} \frac{\zeta^2}{\lambda^2} + \frac{\zeta_v^2}{\lambda^2} \right), \quad (106)$$

$$2v \lim_{\mathbf{k} \rightarrow 0} \langle \mathbf{j}_{\perp}(\mathbf{k}) \cdot \mathbf{j}_{\perp}(-\mathbf{k}) \rangle = V \Delta x^3 \Delta t \left(2 \frac{\zeta^2}{\lambda^2} \right). \quad (107)$$

In the long wavelength limit, the fluctuations in momentum density at each lattice node are independent and can be expressed in terms of the fluctuations in population:

$$\lim_{\mathbf{k} \rightarrow 0} \langle j_{\parallel}(\mathbf{k}) j_{\parallel}(-\mathbf{k}) \rangle = N \langle j^2 \rangle, \quad (108)$$

$$\lim_{\mathbf{k} \rightarrow 0} \langle \mathbf{j}_{\perp}(\mathbf{k}) \cdot \mathbf{j}_{\perp}(-\mathbf{k}) \rangle = 2N \langle j^2 \rangle, \quad (109)$$

where $\langle j^2 \rangle = \frac{1}{3} \sum_i \langle (n'_i)^2 c_i^2 \rangle$ are the fluctuations in momentum density at a single site. Thus we have established a direct connection between the

amplitude of the random stress fluctuations and the fluctuations in momentum at a single site:

$$\zeta = \left(\frac{2N\langle j^2 \rangle v \lambda^2}{V \Delta x^3 \Delta t} \right)^{1/2}, \quad \zeta_v = \left(\frac{2N\langle j^2 \rangle v_v \lambda_v^2}{V \Delta x^3 \Delta t} \right)^{1/2}. \quad (110)$$

In a molecular gas or liquid in thermal equilibrium, the average fluctuation in momentum of a collection of particles of total mass m is $mk_B T$. To make a connection between the strength of the random forcing and the thermodynamic temperature, we take the momentum fluctuations at a lattice node $\langle j^2 \rangle$ to be $mk_B T$, where $m = \rho \Delta x^3$ is the mass associated with each lattice node. This leads immediately to Eq. 91 for the strength of the random stress fluctuations, and shows that the lattice-Boltzmann model is a self-consistent model for the fluctuations of a molecular liquid or gas at scales in between the molecular and the macroscopic.

Thermal fluctuations can therefore be incorporated into a suspension simulation by adding random fluctuations to the stress tensor at each fluid site (Eq. 79). Such simulations satisfy the fluctuation-dissipation relation⁽⁷⁰⁾ (see Fig. 3), and lead to reasonably quantitative calculations of the hydrodynamic transport coefficients.^(70, 109) However, published simulations do not have good equipartition of energy between the particles and fluid; the thermal energy of the particles was typically 15–20% less than that of the fluid.⁽⁷⁰⁾ The inclusion of longitudinal momentum fluctuations should go a long way towards correcting this error. Although the longitudinal fluctuations decay more rapidly than the shear fluctuations (by propagation of sound waves), they still contribute to the instantaneous particle velocity fluctuations and will therefore increase the translational and rotational energy of the solid particles. The expected increase in the thermal energy of the particles is 1 part in 5, approximately the amount required for equipartition.

9. COMPUTATIONAL COSTS

It is difficult to make comparisons of the computational cost of different simulation methods, largely because of ongoing algorithmic improvements; present-day comparisons can easily be made obsolete by some important technical innovation. Nevertheless, we will make some order of magnitude estimates of the computational costs of typical lattice-Boltzmann simulations, which may then be compared with other algorithms. In a dilute suspension (or pure fluid) the computational cost of the particles is negligible. In this case a reasonable source code, written in C or Fortran, but not extensively optimized, runs at about 1.2 MSUPS (Millions of Site

Updates Per Second) on a Dec Alpha EV6 processor (667 MHz). A comparably clocked Pentium processor (600 MHz PIII), runs at about 0.6 MSUPS, or half the speed of the Alpha. The additional overhead imposed by the particles comes largely, but not exclusively, from the solid-fluid boundary conditions, and varies considerably depending on the solid particle size and concentration. Larger particles have a smaller overhead at comparable concentrations, because of the more favorable surface to volume ratio. A typical suspension simulation might run at about 0.3 MSUPS on a Pentium PIII, but for large numbers of small particles, as used in our sedimentation simulations, the speed is more like 0.2 MSUPS. Under extreme conditions the overhead could be as much as a factor of 5, reducing the speed to about 0.1 MSUPS. In our estimates of computational time, we will use a speed of 0.2 MSUPS as typical for a dynamical simulation under conditions where useful data is generated. The speed of the lattice-Boltzmann simulations can of course be enhanced by parallelization. The fluid part of the code is easily parallelized, but the particle part is more complex. With our present implementation a parallelization efficiency of 50% is readily achieved on our 16-processor Beowulf cluster (dual 600 MHz Pentium PIII nodes) and up to 80% efficiency with 4-8 processors. This performance is by no means optimum, and improvements will be made in future.

The speed of the simulation is greatly dependent on the size of the particles; the computational cost scales as the particle size to the 4th power, 3 for the volume and 1 for the time. At low Reynolds numbers, satisfactory results can be obtained with a volume per particle of about 500–1000 lattice nodes, independent of concentration. This translates to a particle radius of about 5 lattice spacings at high solids concentrations (50% by volume) and around 2 lattice spacings at low solids concentrations (10% by volume). We have previously found this to be sufficient to reduce the error in the hydrodynamic interactions to the order of 1%. For large scale simulations at relatively low solids concentrations, the volume per particle can be reduced to as little as 100 lattice nodes, although the errors may then be of the order of 5–10%. In our estimates we will make a conservative choice of 500 lattice nodes per particle.

The most difficult thing to estimate is the number of time steps necessary to move the particles a significant distance. We define the Stokes time, $t_s = a/U$, as the time necessary for a particle to move a distance equal to its radius. In the lattice-Boltzmann method, the time step is fixed and the particle velocity is varied. The maximum velocity that can be reasonably used, while keeping the compressibility artifacts within bounds is $0.1\Delta x/\Delta t$. However, a smaller velocity should be used so that the particles do not change grid positions every few steps. Our simulations use at least 100 steps

per Stokes time ($U \approx 0.01\Delta x/\Delta t$), and we will take 200 steps as a typical number. Thus the computational cost to update N particles for 1 Stokes time comes out to be approximately $0.5N$ seconds. A sedimentation simulation with 30,000 particles for 500 Stokes times therefore takes about 2000 hours of processor time or about 10 days on a 16 cpu cluster running at 50% efficiency.

There are many caveats to this calculation. First the Reynolds number cannot be made very small without substantially increasing the computational cost. The kinematic viscosity of the fluid cannot be increased much above $1\Delta x^2/\Delta t$ without losing accuracy; thus a typical Reynolds number is of order 0.1. The cost of running at very low Re is high, although in some instances this can be improved by using implicit methods.⁽¹²⁰⁾ At high Reynolds number larger particles are necessary,⁽⁶³⁾ again with substantial increases in computer cost. Thus the lattice-Boltzmann simulations are most efficient in the range of Reynolds numbers from about 0.1 to 100. On the other hand, improvements in boundary conditions can reduce the computational cost in porous media simulations by more than a factor of 10.⁽¹²¹⁾ It remains to be seen if these same gains can be realized for particle suspensions. The accuracy of lattice-Boltzmann simulations also falls in a range. It is relatively easy to reduce the errors to 0.1–1%, but it becomes quite costly to try to reduce the errors beyond that, because of the pixelated description of the particle surface. Again it remains to be seen if new boundary conditions can improve this situation.

It can be seen that lattice-Boltzmann methods have a huge computational advantage over Stokesian dynamics in situations where the number of particles is large and the Reynolds number need not be too small. For a system of 10000 particles, the matrix decomposition alone in Stokesian dynamics would require of the order of 10^{15} floating point operations, or times in excess of 10^6 seconds per time step. At least 10 such decompositions would be necessary to follow the system for 1 Stokes time, while a lattice-Boltzmann simulation would require 1–2 hours of cpu time, and perhaps only on the order of 10 minutes using continuous-bounce-back boundary conditions. On the other hand, improvements in the Stokesian dynamics methodology⁽¹¹¹⁾ can reduce the cpu time for such simulations by many orders of magnitude, again to something of the order 10 minutes. In terms of the accuracy of the two methods, Stokesian dynamics is typically more accurate for relative motion of particles, for example a shear flow. This is primarily because the hydrodynamic interactions are dominated by lubrication forces, which are more easily and effectively implemented in Stokesian dynamics. On the other hand, lattice-Boltzmann methods do a much better job of accounting for the relative motion between particle and fluid phases, especially at high density, where

Stokesian dynamics fails to be quantitative unless many more force multi-poles are included.

ACKNOWLEDGMENTS

This manuscript was prepared with financial support from grants from the National Aeronautics and Space Administration (NAG3-2382), and the American Chemical Society Petroleum Research Fund (34142-AC9). Some of the work described here was carried out with support from the US Department of Energy (DE-FG02-98ER14853).

REFERENCES

1. C. K. Aidun and Y. N. Lu, Lattice Boltzmann simulation of solid particles suspended in fluid, *J. Stat. Phys.* **81**:49–61 (1995).
2. C. K. Aidun, Y. N. Lu, and E. Ding, Direct analysis of particulate suspensions with inertia using the discrete Boltzmann equation, *J. Fluid Mech.* **373**:287–311 (1998).
3. R. C. Ball and J. R. Melrose, A simulation technique for many spheres in quasi-static motion under frame-invariant pair drag and Brownian forces, *Physica A* **247**:444–472 (1997).
4. C. W. J. Beenakker, The effective viscosity of a concentrated suspension (and its relation to diffusion), *Physica A* **128**:48–81 (1984).
5. O. P. Behrend, Solid-fluid boundaries in particle suspension simulations via the lattice-Boltzmann method, *Phys. Rev. E* **52**:1164 (1995).
6. R. Benzi, S. Succi, and M. Vergassola, The lattice-Boltzmann equation - Theory and applications, *Phys. Rep.* **222**:145 (1992).
7. H. Binous and R. J. Phillips, The effect of sphere-wall interactions on particle motion in a viscoelastic suspension of FENE dumbbells, *J. Non-Newton. Fluid Mech.* **85**:63–92 (1999).
8. G. A. Bird, *Molecular Gas Dynamics* (University Press, London, Oxford, 1976).
9. L. Bocquet, J. Piasecki, and J.-P. Hansen, On the Brownian motion of a massive sphere suspended in a hard sphere fluid. 1. Multiple-time-scale analysis and microscopic expression for the friction coefficient, *J. Stat. Phys.* **76**:505–526 (1994).
10. G. Bossis and J. F. Brady, Self-diffusion of Brownian particles in concentrated suspensions under shear, *J. Chem. Phys.* **87**:5437 (1987).
11. J. F. Brady, Rheology of concentrated colloidal dispersions, *J. Chem. Phys.* **99**:567–581 (1993).
12. J. F. Brady and G. Bossis, Stokesian dynamics, *Ann. Rev. Fluid. Mech.* **20**:111 (1988).
13. J. F. Brady and J. F. Morris, Microstructure of strongly sheared suspensions and its impact on rheology and diffusion, *J. Fluid Mech.* **348**:103–139 (1997).
14. H. Brenner, The slow motion of a sphere through a viscous fluid towards a plane surface, *Chem. Engng. Sci.* **16**:242–251 (1961).
15. M. P. Brenner, Screening mechanisms in sedimentation, *Phys. Fluids* **11**:754–772 (1999).
16. R. E. Caflisch and J. H. C. Luke, Variance in the sedimentation speed of a suspension, *Phys. Fluids* **28**:759 (1985).
17. A. A. Catherall, J. R. Melrose, and R. C. Ball, Shear thickening and order-disorder effects in concentrated colloids at high shear rates, *J. Rheol.* **44**:1–25 (2000).

18. S. Chapman and T. G. Cowling, *The Mathematical Theory of Non-Uniform Gases* (Cambridge University Press, Cambridge, 1960).
19. H. Chen, Volumetric formulation of the lattice-Boltzmann method for fluid dynamics: Basic Concept, *Phys. Rev. E* **58**:3955–3963 (1998).
20. H. Chen, S. Chen, and W. H. Matthaeus, Recovery of the Navier–Stokes equations using a lattice-gas Boltzmann method, *Phys. Rev. A* **45**:R5339–5342 (1992a).
21. H. D. Chen, C. Teixeira, and K. Molvig, Realization of fluid boundary conditions via discrete Boltzmann dynamics, *Int. J. Mod. Phys. C* **9**:1281–1292 (1998).
22. S. Chen and G. D. Doolen, Lattice Boltzmann method for fluid flows, in *Annual Review of Fluid Mechanics*, J. L. Lumley, M. V. Dyke, and H. L. Reed, eds. (Palo Alto, California, 1998), pp. 329–364.
23. S. Chen, Z. Wang, X. Shan, and G. D. Doolen, Lattice Boltzmann computational fluid dynamics in three dimensions, *J. Stat. Phys.* **68**:379 (1992b).
24. S. Y. Chen, D. Martinez, and R. W. Mei, On boundary conditions in lattice Boltzmann methods, *Phys. Fluids* **8**:2527–2536 (1996).
25. B. Cichocki and R. B. Jones, Image representation of a spherical particle near a hard wall, *Physica A* **258**:273–302 (1998).
26. I. L. Claeys and J. F. Brady, Suspensions of prolate spheroids in Stokes flow. 1. Dynamics of a finite number of particles in an unbounded fluid, *J. Fluid Mech.* **251**:411–442 (1993).
27. R. Cornubert, D. d’Humières, and C. D. Levermore, A Knudsen layer theory for lattice gases, *Physica D* **47**:241 (1991).
28. R. G. Cox, The motion of suspended particles almost in contact, *Int. J. Multiphase Flow* **1**:343–371 (1974).
29. R. I. Cukier, R. Kapral, and J. R. Mehafeey, Kinetic theory of the hydrodynamic interaction between 2 particles, *J. Chem. Phys.* **74**:2494–2504 (1981).
30. B. Dubrulle, U. Frisch, M. Hénon, and J.-P. Rivet, Low-viscosity lattice gases, *Physica D* **47**:27–29 (1991).
31. L. Durlofsky, J. F. Brady, and G. Bossis, Dynamic simulation of hydrodynamically interacting particles, *J. Fluid Mech.* **180**:21 (1987).
32. D. A. Edwards, M. Shapiro, P. Bar-Yoseph, and M. Shapira, The influence of Reynolds number upon the apparent permeability of spatially periodic arrays of cylinders, *Phys. Fluids A* **2**:45 (1990).
33. D. L. Ermak and J. A. McCammon, Brownian dynamics with hydrodynamic interactions, *J. Chem. Phys.* **69**:1352 (1978).
34. J. Feng, H. H. Hu, and D. D. Joseph, Direct simulation of initial-value problems for the motion of solid bodies in a Newtonian fluid. 1. Sedimentation, *J. Fluid Mech.* **261**:95–134 (1994a).
35. J. Feng, H. H. Hu, and D. D. Joseph, Direct simulation of initial-value problems for the motion of solid bodies in a Newtonian fluid. 2. Couette and Poiseuille flows, *J. Fluid Mech.* **277**:271–301 (1994b).
36. O. Filippova and D. Hänel, Grid-refinement for lattice-BGK models, *J. Comput. Phys.* **147**:219 (1998).
37. A. L. Fogelson and C. S. Peskin, A fast numerical method for solving the three-dimensional Stokes equations in the presence of suspended particles, *J. Comput. Phys.* **79**:50 (1988).
38. B. Fornberg, Steady incompressible flow past a row of circular cylinders, *J. Fluid Mech.* **225**:625 (1991).
39. D. R. Foss and J. F. Brady, Structure, diffusion and rheology of Brownian suspensions by Stokesian dynamics simulation, *J. Fluid Mech.* **407**:167–200 (2000).

40. S. Fraden and G. Maret, Multiple light scattering from concentrated, interacting suspensions, *Phys. Rev. Lett.* **65**:512 (1990).
41. U. Frisch, D. d'Humières, B. Hasslacher, P. Lallemand, Y. Pomeau, and J.-P. Rivet, Lattice gas hydrodynamics in two and three dimensions, *Complex Systems* **1**:649 (1987).
42. U. Frisch, B. Hasslacher, and Y. Pomeau, Lattice gas automata for the Navier–Stokes equation, *Phys. Rev. Lett.* **56**:1505 (1986).
43. M. A. Gallivan, D. R. Noble, J. G. Georgiadis, and R. O. Buckius, An evaluation of the bounce-back boundary condition for lattice Boltzmann simulations, *Int. J. Numer. Meth. Fluids* **25**:249–263 (1997).
44. C. K. Ghadder, On the permeability of unidirectional fibrous media: A parallel computational approach, *Phys. Fluids* **7**:2563 (1995).
45. I. Ginzbourg and P. M. Adler, Boundary condition analysis for the three-dimensional lattice-Boltzmann model, *J. Phys. II France* **4**:191 (1994).
46. I. Ginzbourg and D. d'Humières, Local second-order boundary methods for lattice-Boltzmann models, *J. Stat. Phys.* **84**:927 (1996).
47. R. Glowinski, T. W. Pan, T. I. Hesla, D. D. Joseph, and J. Periaux, A distributed Lagrange multiplier/fictitious domain method for the simulation of flow around moving rigid bodies, *Comput. Method Appl Math Engng* **184**:241–267 (2000).
48. A. Greenbaum, *Iterative methods for solving linear systems* (Society for Industrial and Applied Mathematics, Philadelphia, 1997).
49. R. D. Groot and P. B. Warren, Dissipative particle dynamics: Bridging the gap between atomistic and mesoscopic simulation, *J. Chem. Phys.* **107**:4423–4435 (1997).
50. J. P. Hansen and I. R. McDonald, *Theory of Simple Liquids* (Academic Press, London, 1986).
51. J. Happel and H. Brenner, *Low-Reynolds Number Hydrodynamics* (Martinus Nijhoff, Dordrecht, 1986).
52. E. H. Hauge and A. Martin-Löf, Fluctuating hydrodynamics and Brownian motion, *J. Stat. Phys.* **7**:259 (1973).
53. X. He and L.-S. Luo, Lattice-Boltzmann model for the incompressible Navier–Stokes equation, *J. Stat. Phys.* **88**:927 (1997).
54. X. He, Q. Zou, L.-S. Luo, and M. Dembo, Analytic solutions of simple flows and analysis of nonslip boundary conditions for the lattice Boltzmann BGK model, *J. Stat. Phys.* **87**:115–136 (1997).
55. M. W. Heemels, M. H. J. Hagen, and C. P. Lowe, Simulating solid colloidal particles using the lattice-Boltzmann equation, *J. Comput. Phys.* **164**:48–61 (2000).
56. F. Higuera, S. Succi, and R. Benzi, Lattice gas dynamics with enhanced collisions, *Europhys. Lett.* **9**:345 (1989).
57. R. J. Hill, D. L. Koch, and A. J. C. Ladd, Inertial flows in ordered and random arrays of spheres, *J. Fluid Mech.*, Submitted (1999).
58. P. J. Hoogerbrugge and J. M. V. A. Koelman, Simulating microscopic hydrodynamic phenomena with dissipative particle dynamics, *Europhys. Lett.* **19**:155 (1992).
59. W. G. Hoover, T. G. Pierce, C. G. Hoover, J. O. Shugart, C. M. Stein, and A. L. Edwards, Molecular-dynamics, smoothed-particle applied mechanics, and irreversibility, *Comput. Math. Appl.* **28**:155–174 (1994).
60. A. Jasberg, A. Koponen, M. Kataja, and J. Timonen, Hydrodynamical forces acting on particles in a two-dimensional flow near a solid wall, *Comput. Phys. Comm.* **129**:196–206 (2000).
61. D. J. Jeffrey and Y. Onishi, Calculation of the resistance and mobility functions of two unequal rigid spheres in low-Reynolds-number flow, *J. Fluid Mech.* **139**:261 (1984).

62. D. D. Joseph, Y. J. Liu, M. Poletto, and J. Feng, Aggregation and dispersion of spheres falling in viscoelastic liquids, *J. Non-Newton Fluid Mech.* **54**:45–86 (1994).
63. D. L. Koch and A. J. C. Ladd, Moderate Reynolds number flows through periodic and random arrays of aligned cylinders, *J. Fluid Mech.* **349**:31 (1997).
64. D. L. Koch and E. S. G. Shaqfeh, Screening in sedimenting suspensions, *J. Fluid Mech.* **224**:275 (1991).
65. A. Koponen, *Simulations of Fluid Flow in Porous Media by Lattice-Gas and Lattice-Boltzmann Methods*, Ph.D. thesis, University of Jyväskylä, Finland (1998).
66. A. J. C. Ladd, Hydrodynamic interactions in a suspension of spherical particles, *J. Chem. Phys.* **88**:5051 (1988).
67. A. J. C. Ladd, Hydrodynamic transport coefficients of random dispersions of hard spheres, *J. Chem. Phys.* **93**:3484 (1990).
68. A. J. C. Ladd, Short-time motion of colloidal particles: Numerical simulation via a fluctuating lattice-Boltzmann equation, *Phys. Rev. Lett.* **70**:1339 (1993).
69. A. J. C. Ladd, Numerical simulations of particulate suspensions via a discretized Boltzmann equation Part I. Theoretical foundation, *J. Fluid Mech.* **271**:285 (1994a).
70. A. J. C. Ladd, Numerical simulations of particulate suspensions via a discretized Boltzmann equation Part II. Numerical results, *J. Fluid Mech.* **271**:311 (1994b).
71. A. J. C. Ladd, Hydrodynamic screening in sedimenting suspensions of non-Brownian spheres, *Phys. Rev. Lett.* **76**:1392 (1996).
72. A. J. C. Ladd, Sedimentation of homogeneous suspensions of non-Brownian spheres, *Phys. Fluids* **9**:491–499 (1997).
73. A. J. C. Ladd, M. E. Colvin, and D. Frenkel, Application of lattice-gas cellular automata to the Brownian motion of solids in suspension, *Phys. Rev. Lett.* **60**:975 (1988).
74. A. J. C. Ladd and D. Frenkel, Dynamics of colloidal dispersions via lattice-gas models of an incompressible fluid, in *Cellular Automata and Modeling of Complex Physical Systems*, P. Manneville, N. Boccara, G. Y. Vichniac, and R. Bidaux, eds. (Berlin-Heidelberg, 1989), pp. 242–245.
75. A. J. C. Ladd and D. Frenkel, Dissipative hydrodynamic interactions via lattice-gas cellular automata, *Physics of Fluids A* **2**:1921 (1990).
76. A. J. C. Ladd, Effects of container walls on the velocity fluctuations of sedimenting spheres, Unpublished work (2000).
77. L. D. Landau and E. M. Lifshitz, *Fluid Mechanics* (Addison-Wesley, London, 1959).
78. L. D. Landau and E. M. Lifshitz, *Statistical Physics* (Addison-Wesley, Reading, Massachusetts, 1969).
79. C. E. Leith, Stochastic backscatter in a subgrid-scale model - Plane shear mixing layer, *Phys. Fluids A* **2**:297–299 (1990).
80. A. Levine, S. Ramaswamy, E. Frey, and R. Bruinsma, Screened and unscreened phases in sedimenting suspensions, *Phys. Rev. Lett.* **81**:5944 (1998).
81. M. Loewenberg and E. J. Hinch, Numerical simulation of a concentrated emulsion in shear flow, *J. Fluid Mech.* **321**:395–419 (1996).
82. C. P. Lowe and D. Frenkel, Short-time dynamics of colloidal suspensions, *Phys. Rev. E* **54**:2704–2713 (1996).
83. C. P. Lowe, D. Frenkel, and A. J. Masters, Long-time tails in angular momentum correlations, *J. Chem. Phys.* **103**:1582–1587 (1995).
84. J. H. C. Luke, Decay of velocity fluctuations in a stably stratified suspension, *Phys. Fluids*. **12**:1619–1621 (2000).
85. L.-S. Luo, Unified theory of lattice Boltzmann models for nonideal gases, *Phys. Rev. Lett.* **81**:1618–1621 (1998).

86. A. Madja, *Compressible Fluid Flow and Systems of Conservation Laws in Several Space Dimensions* (Springer-Verlag, New York, 1984).
87. R. S. Maier, R. S. Bernard, and D. W. Grunau, Boundary conditions for the lattice Boltzmann method, *Phys. Fluids* **8**:1788–1801 (1996).
88. D. O. Martinez, W. H. Matthaes, S. Chen, and D. C. Montgomery, On boundary conditions in lattice Boltzmann methods, *Phys. Fluids* **6**:1285–1298 (1994).
89. G. R. McNamara and B. J. Alder, Analysis of the lattice Boltzmann treatment of hydrodynamics, *Physica A* **194**:218 (1993).
90. G. R. McNamara and G. Zanetti, Use of the Boltzmann equation to simulate lattice-gas automata, *Phys. Rev. Lett.* **61**:2332 (1988).
91. R. W. Mei, L. S. Luo, and W. Shyy, An accurate curved boundary treatment in the lattice Boltzmann method, *J. Comput. Phys.* **155**:307–330 (1999).
92. J. R. Melrose and R. C. Ball, The pathological behavior of sheared hard-spheres with hydrodynamic interactions, *Europhys. Lett.* **32**:535–540 (1995).
93. J. J. Monaghan, Smoothed particle hydrodynamics, *Annu. Rev. Astron. Astr.* **30**:543–574 (1992).
94. J. P. Morris, P. J. Fox, and Y. Zhu, Modeling Low Reynolds Number Incompressible Flow Using SPH, *J. Comput. Phys.* **136**:214–226 (1997).
95. G. P. Muldowney and J. J. L. Higdon, A spectral boundary-element approach to 3-dimensional Stokes flow, *J. Fluid Mech.* **298**:167–192 (1995).
96. N.-Q. Nguyen and A. J. C. Ladd, Lubrication forces in lattice-Boltzmann simulations, Unpublished work (2000).
97. H. Nicolai and E. Guazzelli, Effect of the vessel size on the hydrodynamic diffusion of sedimenting spheres, *Phys. Fluids* **7**:3 (1995).
98. D. R. Noble, S. Y. Chen, J. G. Georgiadis, and R. O. Buckius, A consistent hydrodynamic boundary-condition for the lattice Boltzmann method, *Phys. Fluids* **7**:203–209 (1995).
99. S. A. Orszag and V. Yakhot, Reynolds-number scaling of cellular-automaton hydrodynamics, *Phys. Rev. Lett.* **56**:1691–1693 (1986).
100. H. C. Öttinger, *Stochastic Processes in Polymeric Fluids* (Springer-Verlag, Berlin, 1996).
101. T. N. Phung, J. F. Brady, and G. Bossis, Stokesian dynamics simulation of Brownian suspensions, *J. Fluid Mech.* **313**:181–207 (1996).
102. C. Pozrikidis, On the transient motion of ordered suspensions of liquid drops, *J. Fluid Mech.* **246**:301–320 (1993).
103. D. W. Qi, Lattice Boltzmann simulations of particles in nonzero Reynolds number flows, *J. Fluid Mech.* **385**:41–62 (1999).
104. Y. H. Qian, D. d'Humières, and P. Lallemand, Lattice BGK models for the Navier-Stokes equation, *Europhys. Lett.* **17**:479–484 (1992).
105. S. R. Rastogi, N. J. Wagner, and S. R. Lustig, Rheology, self-diffusion, and microstructure of charged colloids under simple shear by massively parallel nonequilibrium Brownian dynamics, *J. Chem. Phys.* **104**:9234–9248 (1996).
106. D. H. Rothman, Cellular-automaton fluids: a model for flow in porous media, *Geophys.* **53**:509–518 (1988).
107. A. S. Sangani and A. Acrivos, Slow flow past periodic arrays of cylinders with application to heat transfer, *Int. J. Multiphase Flow* **8**:193 (1982).
108. A. S. Sangani and G. B. Mo, An O(N) algorithm for Stokes and Laplace interactions of particles, *Phys. Fluids* **8**:1990–2010 (1996).
109. P. N. Segré, O. P. Behrend, and P. N. Pusey, Short-time Brownian motion in colloidal suspensions-Experiment and simulation, *Phys. Rev. E* **52**:5070–5083 (1995).

110. P. N. Segré, E. Herbolzheimer, and P. M. Chaikin, Long-range correlations in sedimentation, *Phys. Rev. Lett.* **79**:2574 (1997).
111. A. Sierou and J. F. Brady, Accelerated Stokesian dynamics simulations, *J. Fluid Mech.* (2001).
112. P. A. Skordos, Initial and boundary conditions for the lattice Boltzmann method, *Phys. Rev. E* **48**:4823–4842 (1993).
113. J. A. Somers and P. C. Rem, in *Shell Conference on Parallel Computing*, G. A. van der Zee, ed. (1988).
114. P. Tong and B. J. Ackerson, Analogies between colloidal sedimentation and turbulent convection at high Prandtl numbers, *Phys. Rev. E* **58**:R6931–R6934 (1998).
115. S. O. Unverdi and G. Tryggvason, A front-tracking method for viscous, incompressible, multi-fluid flows, *J. Comput. Phys.* **100**:25–37 (1992).
116. M. A. van der Hoef, D. Frenkel, and A. J. C. Ladd, Self-diffusion of colloidal particles in a two-dimensional suspension: are deviations from Fick's law experimentally observable?, *Phys. Rev. Lett.* **67**:3459 (1991).
117. J. C. van der Werff and C. G. de Kruiff, Hard-sphere colloidal dispersions: the scaling of rheological properties with particle size, volume fraction, and shear rate, *J. Rheol.* **33**:421 (1989).
118. J. C. van der Werff, C. G. de Kruiff, C. Blom, and J. Mellema, Linear viscoelastic behavior of dense hard-sphere dispersions, *Phys. Rev. A* **39**:795–807 (1989).
119. R. Verberg, I. M. de Schepper, and E. G. D. Cohen, Viscosity of colloidal suspensions, *Phys. Rev. E* **55**:3143–3158 (1997).
120. R. Verberg and A. J. C. Ladd, Simulation of low-Reynolds-number flow via a time-independent lattice-Boltzmann method, *Phys. Rev. E* **60**:3366–3373 (1999).
121. R. Verberg and A. J. C. Ladd, Lattice-Boltzmann model with sub-grid scale boundary conditions, *Phys. Rev. Lett.* **84**:2148–2151 (2000a).
122. R. Verberg and A. J. C. Ladd, Simulations of erosion in narrow fractures, *Water Resources Res.*, Submitted: Preprint at <http://www.che.ufl.edu/ladd/publications/wrr00.pdf> (2000b).
123. D. A. Weitz, D. J. Pine, P. N. Pusey, and R. J. A. Tough, Nondiffusive Brownian motion studied by Diffusing-Wave Spectroscopy, *Phys. Rev. Lett.* **63**:1747 (1989).
124. Y. Zhu, P. J. Fox, and J. P. Morris, A Pore-Scale Numerical Model for Flow through Porous Media, *Int. J. Numer. Anal. Methods Geomech.* **23**:881–904 (1999).
125. J. X. Zhu, D. J. Durian, J. Müller, D. A. Weitz, and D. J. Pine, Scaling of transient hydrodynamic interactions in concentrated suspensions, *Phys. Rev. Lett.* **68**:2559 (1992).
126. D. P. Ziegler, Boundary conditions for lattice-Boltzmann simulations, *J. Stat. Phys.* **71**:1171–1177 (1993).
127. A. Z. Zinchenko and R. H. Davis, An efficient algorithm for hydrodynamical interaction of many deformable drops, *J. Comput. Phys.* **157**:539–587 (2000).